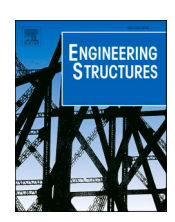
ELSEVIER

Contents lists available at ScienceDirect

Engineering Structures

journal homepage: www.elsevier.com/locate/engstruct





Elevated light-frame wood residential building physical and numerical modeling of damage due to hurricane overland surge and waves

Mohammad S. Alam ^a, Andre R. Barbosa ^{b,*}, Ignace Mugabo ^c, Daniel T. Cox ^d, Hyoungsu Park ^e, Dayeon Lee ^f, Sungwon Shin ^f

- ^a Postdoctoral Research Associate, Dept. of Civil and Environmental Engineering and Earth Sciences, Univ. of Notre Dame, Notre Dame, IN 46556; formerly, Postdoctoral Scholar, School of Civil and Construction Engineering, Oregon State Univ., Corvallis, OR 97330
- ^b Glenn Willis Holcomb Professor in Structural Engineering, School of Civil and Construction Engineering, Oregon State University, Corvallis, OR 97331, USA
- ^c Structural Engineer, KPFF Consulting, Portland, OR 97331, USA
- ^d School of Civil and Construction Engineering, Oregon State University, Corvallis, OR 97331, USA
- ^e Department of Civil and Environmental Engineering, University of Hawaii at Manoa, Honolulu, HI, 96822, USA
- f Department of Marine Science and Convergence Engineering, Hanyang University, ERICA, South Korea

ARTICLE INFO

Keywords: Damage progression Destructive hydrodynamic tests Elevated wood-frame building Finite element model updating System identification Wave and surge overland flow

ABSTRACT

An experimental program of a 1:6 scale elevated wood frame shear-wall residential building was developed to model the damage progression of buildings subjected to increasing hurricane surge depth and wave conditions until collapse. This paper presents testing and system identification methods used to characterize structural engineering properties of the physical model that accumulated damage during hydrodynamic testing under increasing surge depth and wave heights. Methods used include (a) quasi-static lateral load-deformation testing, (b) out-of-water dynamic structural characterization testing under free vibration, ambient vibration, and forced vibration, conducted on the test specimen prior to hydrodynamic testing, (c) in-water dynamic structural characterization during hydrodynamic testing, (d) quantification of accumulated damage in hydrodynamic testing through observed changes in the laser scan point cloud data of the specimen, and (e) finite element model updating. The accumulated damage in the test specimen is correlated to changes in modal features (frequency, damping, and mode shapes) assessed using two output-only system identification (SID) methods. In addition, finite volume numerical models are used to determine detailed pressure distributions on the test specimen which are coupled with finite element (FE) models that are updated, in a phased manner, to understand the contribution of structural and nonstructural components on the modeled stiffness and strength of the physical model. Lastly, the impact of the damage on the modal features of the physical model of the building and their sensitivity to FE model assumptions are presented.

1. Introduction

Coastal communities worldwide have suffered significant losses due to a variety of natural disasters, such as tropical cyclones [28], hurricane-induced storm surges and waves [58,35,21], and tsunamis [61,50,16]. Future economic losses from such disasters will likely increase due to continued population influx to coastal communities, climate change induced sea level rise, and coastal erosion [44,46]. The National Hurricane Center (NHC) of the National Oceanic and Atmospheric Administration (NOAA) provides evidence of increasing economic losses during the period of 2012–2017 [52], which spans the period of four of the most damaging hurricanes (2012 Hurricane Sandy,

2017 Hurricane Harvey, 2017 Hurricane Maria, 2017 Hurricane Irma) in the US history. Therefore, to mitigate the damage and loss to coastal infrastructure, it is paramount that objective damage quantification can be achieved through physical and numerical modeling of coastal infrastructure when subjected to hurricane surge and wave loading.

Damage to coastal buildings due to hurricane waves and surge has been studied extensively through reconnaissance studies and hydrodynamic modeling of hurricane storm surge and wave event hindcasting. Tomiczek et al. [64] investigated the effects of hurricane-generated storm surges and waves on elevated wood-frame coastal buildings with pile foundations in Bolivar Peninsula, TX, in the aftermath of the 2008 Hurricane Ike. Using wave height and surge level data estimated

E-mail address: andre.barbosa@oregonstate.edu (A.R. Barbosa).

^{*} Corresponding author.

through hindcasting and field survey damage data, Kennedy et al. [35] identified important structural characteristics and wave parameters affecting the performance of elevated building archetypes. Results indicated that freeboard (distance between lowest horizontal structural member, LHSM, and wave crest), wave height, wave velocity, and building construction era were the most important factors affecting elevated building performance under combined wave and storm surge. In addition, results in Kennedy et al. [35] indicated that depth-damage curves proposed in FEMA P-55 [24] for coastal V-Zone, which does not account for wave action, were unable to adequately predict the actual damage observed for wooden-frame, pile-elevated coastal residential building archetypes during Hurricane Ike. This lack of predictive capability of depth-damage curves was attributed to large forces imparted in buildings by a combination of smaller surge levels and large waves rather than those due to large surge levels and smaller waves.

The vulnerability of residential structures following 2012 Hurricane Sandy was investigated by various researchers [73,31,30,65]. General observations in these studies include widespread failure of closed foundation buildings and significant damage to exterior walls due to surge loads and debris impact. It has also been observed that building performance in a building array within a community is strongly influenced by the distance of the buildings from the coast, elevation above ground, building age, and flow shielding and channeling due to the presence of neighboring buildings [73,31]. Hatzikyriakou & Lin [30] investigated the impact of wave action on the vulnerability of structures using different hydrodynamic models to simulate inland storm surge flooding in Ortley Beach, New Jersey, during 2012 Hurricane Sandy. Results indicated that hazard characteristics such as wave height and flow velocity are dominant predictors of structural damage, which is consistent with observations in Tomiczek et al. [65]. Using local-scale and regional-scale damage surveys and hydrodynamic modeling of Hurricane Sandy, Tomiczek et al. [65] developed a damage classification methodology and fragility functions for existing residential buildings on the New Jersey coast. Fragility models developed in the study further revealed that building shielding was a critical predictor of damage.

Besides empirical studies, experimental and numerical investigations of the response of elevated buildings under wave loading have gained interest in the research community (e.g., pressures and forces on an isolated building: [53,66,3,57]; effect of flow shielding and channeling: [71,47]; debris impact: [62,63]. However, only a very limited number of studies have focused on building-specific performance assessment of wood frame buildings or their components under surge and wave loading, such as those originating from hurricane storm surge and waves or tsunami waves (e.g., physical testing and numerical modeling: [77,74,70,68,18]; physical testing: [39,23].

In a laboratory test on breakaway wall behavior under wave loading, Yeh et al. [74] evaluated the ultimate strength of the nailed connections in wood stud breakaway walls, typically used in the space between the first floor and the ground of elevated residential buildings in coastal areas. Moreover, behavior and failure modes of the full-scale breakaway walls under wave actions were evaluated analytically and through destructive hydrodynamic testing under unbroken, broken, and breaking waves. Results of the study indicated that the breakaway walls are most likely to fail at connections at the base of the wall. Wilson et al. [70] investigated the effects of tsunami waves on a 1:6 scale at-grade two-story wood frame residential building using two building configurations relative to wave directions (parallel and perpendicular to flow) and wave conditions. Uplift forces were measured in the experiment for both flooded and non-flooded conditions under solitary wave heights ranging from 0.1 m to 0.6 m. Force distributions were found to vary across the structure due to variations in the stiffness of components. In addition, unanticipated loading conditions were observed in the structure due to the presence of architectural features such as overhanging eaves above the garage as well as reentrant corners. Van de Lindt et al. [68] performed pushover tests on nominally identical 1:6 scale models

in Wilson et al. [70] to determine the lateral base shear versus lateral deformation relationship of these scaled models. The experimental base shear versus deformation results were used to develop a numerical model of the building in the SAPWood [54] software. The SAPWood model was then used with the hydrodynamic test results of Wilson et al. [70] in the calibration of a simplified force equation of tsunami bore impact proposed in the City and County of Honolulu Building Code [15] for wave heights between 0.2 m and 0.6 m.

In a separate set of studies that involved physical testing, Linton et al. [39] investigated the structural response (horizontal force, deflection, and pressure) of full-scale light-frame wood walls for flexible and stiff wood wall framing configurations under tsunami-like wave loading. Results indicated that flexible walls sustained lower peak forces compared to stiffer walls, under similar loading conditions, and stiff walls were able to withstand large wave forces before failure. To overcome the limitation of performing hydrodynamic testing of full-scale building structures in a wave basin due to physical constraints of the experimental facility, Linton et al. [38] performed out-of-water structural testing of shear walls in both in-plane and out-of-plane directions and full-scale wood-frame building system under varying lateral loads to better understand the contribution of individual components to system response under tsunami loading. Results indicated that stiffness and ultimate capacity of shear walls are a function of wave height, which is consistent with the pushover response of buildings observed in tsunami fragility function development through numerical modeling in Alam et al. [2]. In addition, in Linton et al. [38], the ultimate capacity of individual walls was higher than the capacity of the full-structural system and the out-of-plane wall behaved essentially as a one-way slab system in the direction perpendicular to wave impact.

At the time of writing this paper, no testing was found in the literature that focused on vibration characteristics and accelerations of the physical models of elevated light-frame wood buildings subjected to hurricane-induced surge and wave loading. In contrast, extensive literature exists on vibration and seismic performance assessment of timber buildings (e.g., [25–27,76,22,69,56,45,59,55,67,48,49,10,4]), including influence of non-structural wall elements in the vibration assessment and finite element modeling updating [4,48].

In addition, there is extensive literature on the use of enhanced frequency domain decomposition (EFDD) and stochastic subspace identification (SSI) output-only methods in system identification (SID) of dynamic parameters of structural systems (e.g., [45,48,49]) as well as to support linear and nonlinear finite element (FE) model updating (e.g., [7,6,48]). Both EFDD and SSI output-only methods are also used in this study and the reader is directed to Moaveni et al. [45] for more information on these methods.

The current study aims to develop unique benchmark testing methods and data on physical models of residential buildings subjected to hurricane-induced storm surge and wave loading. The work presented in this study is based on a destructive hydrodynamic experiment performed on a 1:6 scale physical model (referred to hereafter as test specimen) of a light-frame wood shear wall elevated residential building. Testing was performed in the Directional Wave Basin (DWB) at Oregon State University (OSU) under hurricane wave and surge overland flow [23]. Readers are directed to Duncan et al. [23] for an overview of the experimental program that included physical model development, estimation of pressure and forces on the specimen, as well as progressive damage assessment under increasing hydrodynamic loading through correlation of laser scan collected point cloud data to damage to nonstructural and structural elements. This paper focuses on the structural characterization (frequency, damping, and mode shapes) and damage progression assessment of the physical model to allow structural and coastal engineers and numerical modelers to replicate test results and understand the effects of hurricane surge and wave on elevated structures.

The overarching goal of this paper is to present experimental and numerical methods that can be used in the characterization of the acceleration response and damage of structures tested to collapse when subjected to hurricane surge and waves, especially in a laboratory setting. To achieve this goal, Section 2.1 of the paper provides details of the physical model of the test specimen that was subjected to surge and wave loading in the DWB at OSU. Section 2.2 describes the experimental methods used in the testing program, including scaled test walls quasistatic lateral load-deformation testing, out-of-water dynamic structural characterization testing, and in-water hydrodynamic testing. Section 2.3 describes the numerical methods used, including system identification (SID), finite volume numerical modeling of the hydrodynamic experiment, and finite element (FE) model updating methods needed to characterize the evolution of dynamic properties of the test specimen and to develop a model that simulates effects of damage accumulation in the test specimen due to increasing surge depth and wave height. Section 3 presents the results and discussion of the experimental and numerical modeling performed, Lastly, section 4 presents the main findings, limitations of the study, and topics for future research. The combined finite volume CFD simulation of the hydrodynamic experiment and multiphase FE modeling of the test specimen adopted in this study can be further extended to develop hurricane surge and wave fragility functions of coastal elevated light-frame wood residential buildings that can help with mitigation planning for enhancing coastal community hurricane disaster resilience [1,19].

2. Materials and methods

Several experimental and numerical methods were used in this study to characterize the damage progression of the 1:6 scale physical model of the elevated light-frame wood shear wall building, also referred to as test specimen herein, when subjected to increasing hurricane-induced surge and wave loading. In this section, a summary of the test specimen used in this study is provided first. Then, the experimental methods used to characterize the dynamic properties of the test specimen performed in both out-of-water (free vibration, ambient vibration, forced vibration) and in-water (destructive hydrodynamic testing) conditions are described. Finally, the section ends with a detailed description of the methods used in the development of a validated FE model based on the correlation between the SID and damage progression of the physical and numerical models.

2.1. Physical model of the elevated light-frame wood building

The physical model of the elevated light-frame wood shear wall building tested in this experiment was based on the design and construction found in typical residential structures in Ortley Beach, New Jersey. Through inspection of buildings in Ortley Beach, the ratio of the dimensions of the ocean-facing front to the side of the buildings was observed to be approximately 3:2 [23]. The specimen was constructed following International Residential Code [33] and FEMA Coastal Construction Manual (CCM- [24]), except that all framing members of the full-scale prototype building were "2 by 4" studs with actual dimensions of 3.8 cm \times 8.9 cm (1.5 in \times 3.5 in) spaced at 40.6 cm (16 in) on-center, with double studs at each end of the wall and at openings, replicating member sizes typically used in existing buildings. In other words, the test specimen was built considering a length scale of 1:6.

Fig. 1 shows the plan and elevation view of the 1:6 scale test specimen. Fig. 2 illustrates details of the specimen during construction. The specimen was constructed to be 1.22 m by 1.83 m (4 ft \times 6 ft), which is equivalent to a 7.32 m by 11 m (24 ft \times 36 ft) in the full-scale archetype. In addition, the nailing pattern of the scaled specimen was adapted such

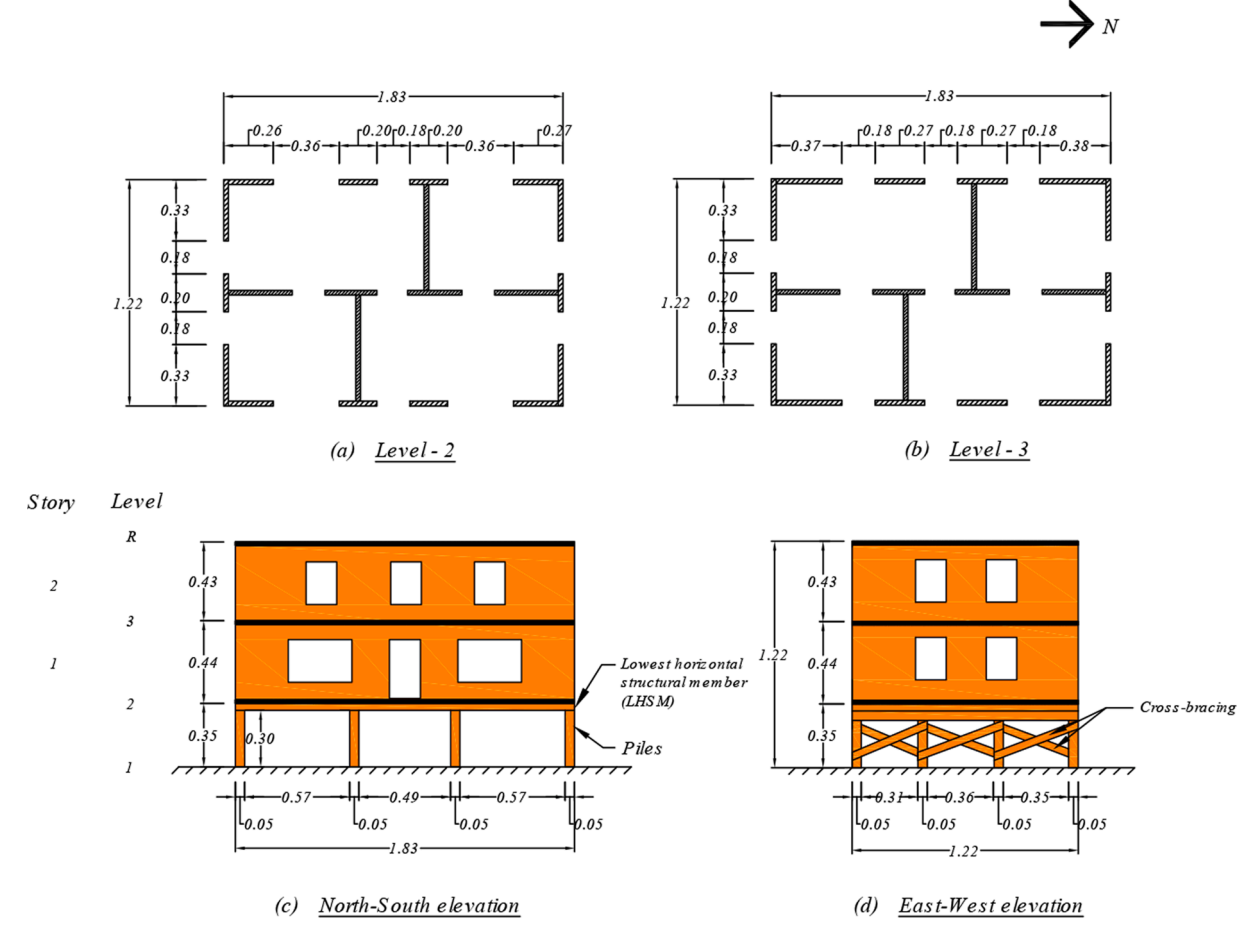


Fig. 1. Plan views [(a) and (b)] at various floor levels and elevation views [(c) and (d)] of the test specimen. Dimensions are in meters.

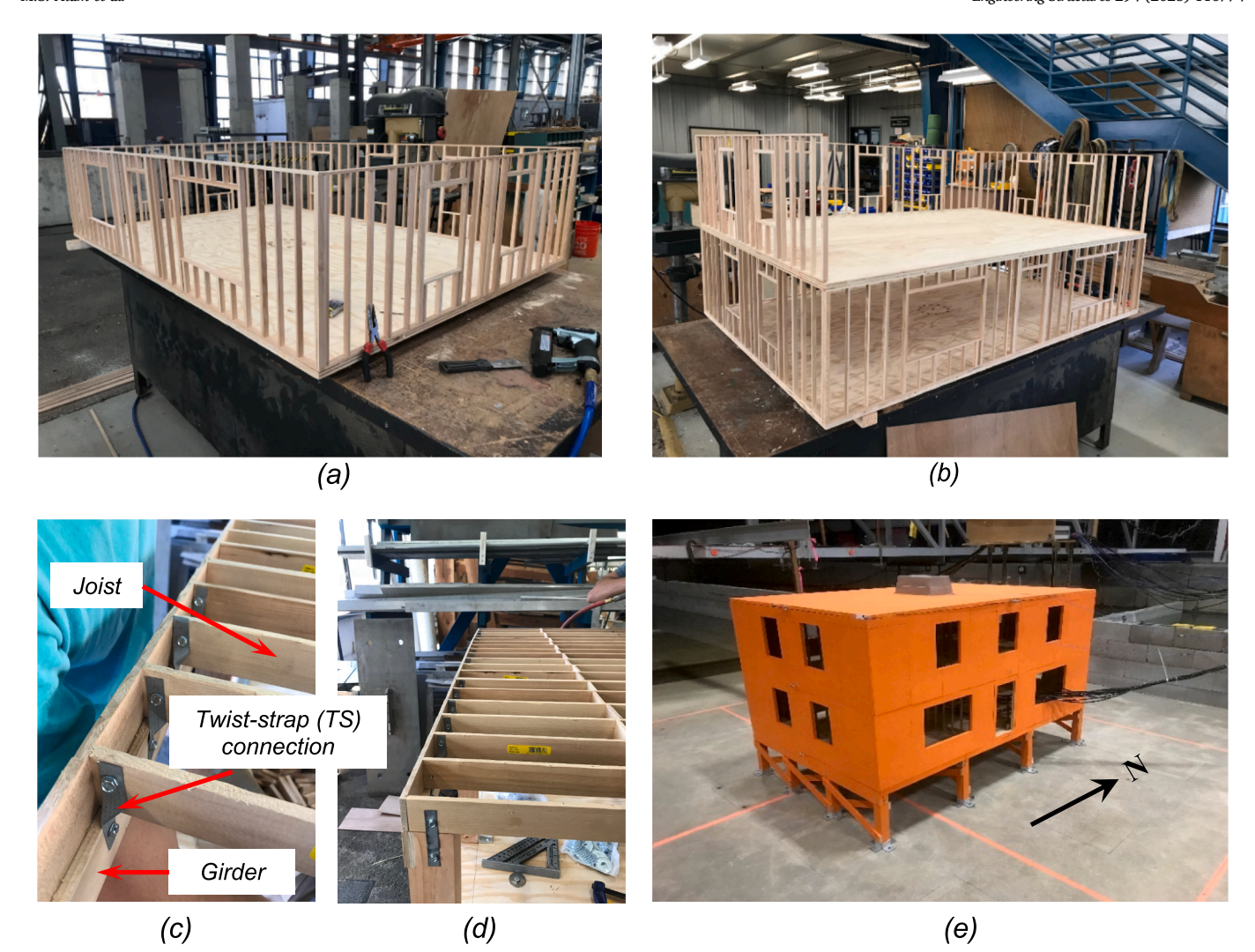


Fig. 2. Digital images of the physical model of the test specimen under construction: (a) views of the first story, (b) second story, (c) detailed, zoomed in view of joist to girder connections at floor Level 2, (d) view of the South-East (SE) corner of the specimen, and (e) test specimen assembled on the wave basin floor.

that the strength and stiffness of the specimen were approximately scaled when compared to the expected properties of the prototype specimen. At 1:6 scale, the 2 by 4 studs had cross-section dimensions of 0.64 cm \times 1.47 cm (0.25 in \times 0.58 in). Plywood sheathing was used on all exterior walls, which were scaled from standard 1.22 m \times 2.44 m (4 ft \times 8 ft) sheets to 3.15 cm \times 6.30 cm (8 in \times 16 in) sheets. Each scaled sheet was cut from approximately 0.3 cm (1/8 in) thick Lauan plywood. At full scale, this resulted in a slightly thicker 1.9 cm (0.75 in) thick sheathing instead of 1.27 cm (0.5 in) specified as the minimum thickness in US codes.

Similar to the sheathing, nail diameter and spacing could not be perfectly scaled due to the unavailability of small-scale nails and nail guns. A 12.7 mm (0.5 in) micro-pin nail gun capable of shooting 23-gauge nails (thickness: 0.71 mm [0.028 in]) was used for the nails. Thus, the nails in the test specimen were 28% thicker and 16% longer at full-scale than standard 8d nails recommend in US codes. To better understand the effect of the sheathing and nailing pattern chosen on the strength and stiffness of the test specimen, 12 test walls measuring 40.6 cm \times 40.6 cm (16 in \times 16 in), which is 2.44 m \times 2.44 m (8 ft \times 8 ft) at full-scale, were constructed with the same framing and sheathing members used on the test specimen construction. Lateral quasi-static load-deformation tests were performed on the test walls as described in the methods section 2.2.1. In the end, based on the results of the quasi-static tests, a 5.1 cm (2.0 in) nail spacing on-center, which is 30.5 cm (12 in) spacing at full-scale, was used for both edge and field nail

patterns.

2.2. Experimental methods

2.2.1. Test walls: Scaled shear wall quasi-static lateral load-deformation testing

Twelve test walls (TWs) measuring 40.6 cm \times 40.6 cm (16 in \times 16 in) were evaluated under in-plane quasi-static lateral loading to develop lateral load-deformation relationships and quantify the lateral stiffness of the scaled walls. Fig. 3 shows the test walls and test assembly used to perform the quasi-static lateral load-deformation tests. The testing apparatus included two wooden boards (2 by 4 guides noted in Fig. 3b) on either side of the subassembly to prevent out-of-plane bending. The lateral load was applied with a crank (turn screw in Fig. 3b) attached to an in-line load cell. The lateral motion was measured with a displacement sensor (string potentiometer) located on the opposite side of the subassembly as that of the load cell.

2.2.2. Test specimen: Out-of-water dynamic structural characterization testing

Several experimental methods were applied to characterize the structural properties and perform the SID of the test specimen. The methods include combined lateral force and free vibration pluck tests, ambient vibration tests, and forced vibrations tests. The experimental data for the structural tests can be found in Barbosa et al. [9]. In the

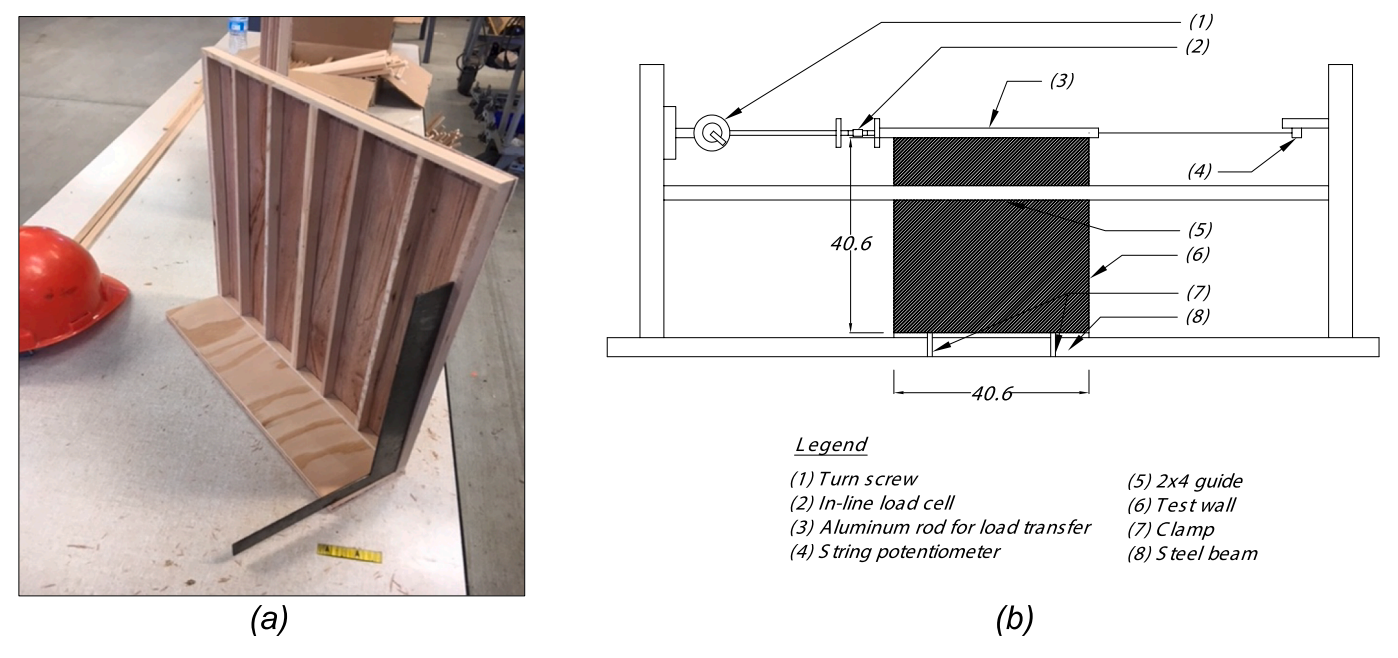


Fig. 3. Test wall (TW) subassembly testing under lateral quasi-static loading: (a) $40.6 \text{ cm} \times 40.6 \text{ cm}$ (16 in) test walls with standard size orange hard hat shown for illustrating the scale, (b) quasi-static lateral load-deformation test setup. Dimensions are in centimeters.

combined lateral force and free vibration tests, a lateral force was applied at the roof level of the test specimen using a turn screw and guy wire and pulley system. The guy wire and pulley system were attached to a crane at one end and at the roof level at another end. The applied load was measured using an in-line load cell attached to the guy wire and pully system. String potentiometers were attached between the floor levels of the test specimen and a rigid column that was fixed at the wave basin to measure lateral displacements at different floor levels. At the end of the lateral load-deformation tests, the guy wire was cut inducing the test specimen to vibrate freely until lateral motions were damped

out. The lateral loads and free vibration tests were performed in the NS and in the EW directions, with five trials conducted for each direction. For this series of tests, triaxial accelerometers were placed at Level-3 and roof level to record the acceleration response of the test specimen under free vibration.

In addition to the free vibration tests, several ambient vibrations and forced vibration tests were performed using excitation functions with varying amplitudes, including white noise and ramp function excitations. For these tests, 13 uniaxial PCB model 393B04 accelerometers were attached to the test specimen: six (6) on the roof level, six (6) on

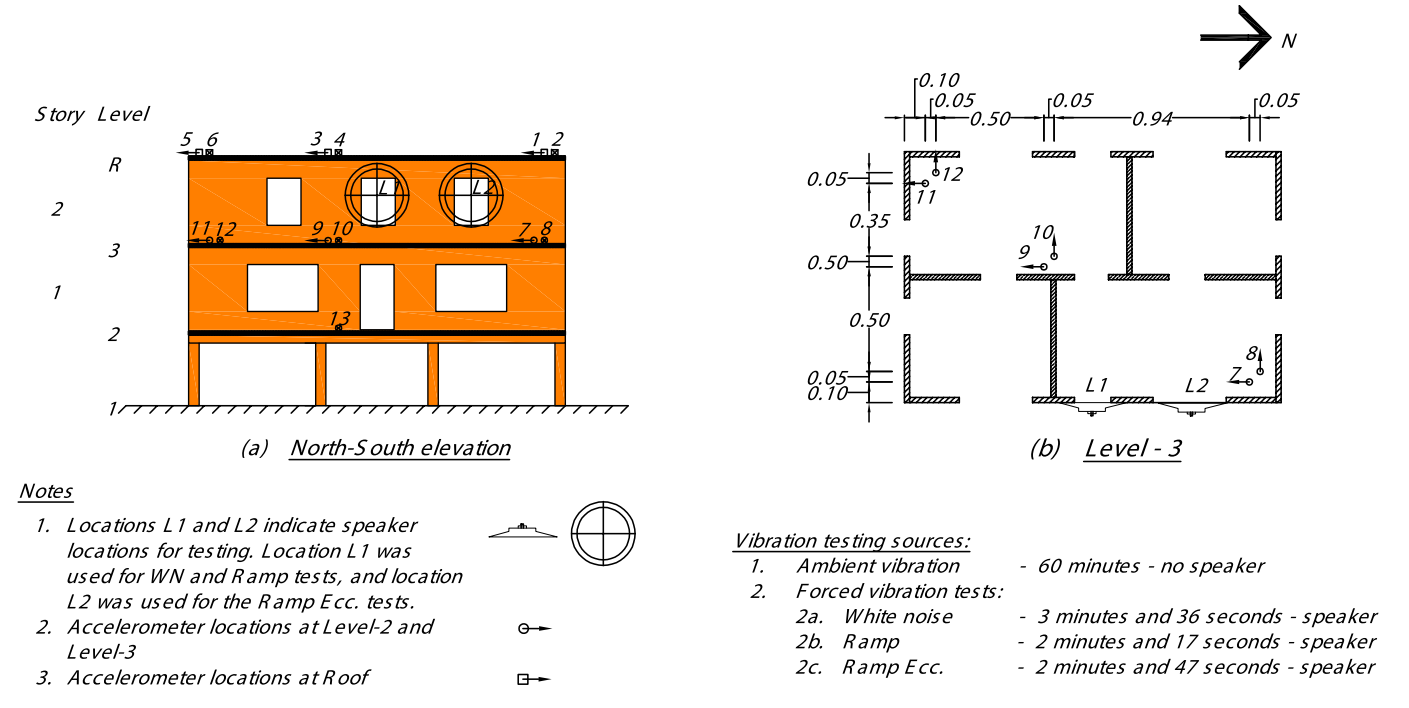


Fig. 4. Locations of accelerometers and positioning of excitation source used in the forced vibration tests: (a) NS elevation view, and (b) Level-3 plan view. Accelerometer locations indicated were used for both out-of-water ambient vibration and forced vibration testing. Accelerometer orientations at the roof level are not shown in the plan but are identical to the ones shown for Level-3. All dimensions are in meters.

Level-3, and one (1) on Level-2. The locations and orientations of the accelerometers used on the roof and Level-2 are shown in Fig. 4. The accelerometer placed on Level-2 was placed approximately at the planar center of the test specimen and was oriented in the EW direction. The accelerometers were connected to a portable data acquisition system (National Instruments, NI cDAQ-9174), which in turn was operated by a laptop equipped with National Instruments Signal Express software [51]. The ambient vibration (AV) tests were conducted first. During AV testing, the acceleration data were recorded for a duration of 60 min. For the remainder of the out-of-water dynamic forced vibration tests, a Tektronix CFG250 function generator with a frequency generation range of 0.20-20 Hz was attached to a Clark Synthesis TST429 platinum model transducer with a frequency response range of 5 Hz -17 kHz. White noise (WN), concentric ramp (Ramp), and eccentric ramp (Ramp Ecc.) functions were applied and acceleration data was recorded for durations between two to four minutes. For the white noise (WN) and concentric ramp (Ramp) functions, the speaker was placed at the mid-height of the second story, and concentric to the structure in the NS direction (location L1 in Fig. 4). In the last dynamic test, Ramp Ecc., the speaker was placed eccentrically with the NS direction, at approximately halfway between the center and the edge of the test specimen (location L2 in Fig. 4).

2.2.3. Test Specimen: In-water hydrodynamic testing

Destructive hydrodynamic testing on the test specimen was performed in the DWB at OSU. A summary of the hydrodynamic testing is provided in this section, but readers are referred to Duncan et al. [23] for further details on the instrumentation plan. Fig. 5 shows the plan and elevation view of the experimental configurations used in the DWB to mimic an idealized section of the New Jersey coastline with residential buildings. The basin was 49.4 m long, 26.5 m wide, and 2.13 m deep with a multi-directional piston-type wavemaker. The test section for the experiment started at 9.75 m from the wavemaker and was 10 m wide and consisted of a 20 m, 1:20 sloped section that approximated the

alongshore uniform bathymetry of the New Jersey shoreline near Ortley Beach. The sloped section led to a 10 m long flat section elevated 1.0 m above the floor of the basin to represent the flat barrier island where Ortley Beach is located. The test specimen was located on the flat section of the testbed 3.5 m from the shore break. At 1:6 scale, this corresponds to 21 m (69 ft) from the shoreline. Several instrumentations were used in the experiment, including nine wire resistance wave gauges located offshore, eight ultrasonic wave gauges located onshore near the test specimen, four acoustic-doppler velocimeters, and two PCB model 356A12 tri-axial accelerometers located at Level-3 and roof of the test specimen. The hydrodynamic test data and specimen details are available in Cox et al. [20] and Barbosa et al. [9].

The destructive hydrodynamic tests were performed using regular waves with a predominant period of $T=4.5\,\mathrm{s}$, which is equivalent to 11 s at the prototype scale, for the majority of the trials. In total, 21 trials were performed. Approximately 40 regular waves were generated during each trial, which lasted about three minutes. Regular waves were used in the study to easily identify the wave conditions (breaking, broken, unbroken) causing the specimens to fail.

Table 1 provides a summary of the wave conditions used in the hydrodynamic testing. The water depth at the wavemaker, h_0 , varied during the study, ranging between 1.10 m and 1.45 m. The test specimen was in a section that was elevated 1.0 m above the basin floor, resulting in water depth at the specimen, h, ranging from 0.10 m to 0.45 m. These varying water depth conditions resulted in different wave-breaking conditions at the test specimen location, including broken, breaking, and nonbreaking wave conditions. The fourth column lists the air gap, a, defined as the elevation of the bottom of the lowest horizontal structural member (LHSM) of the elevated specimen relative to the still water level. The cumulative number of waves that interacted with the specimen, N_{WE} is also listed in Table 1. The regular waves used in the experiment were characterized by the nominal input wave height at the wavemaker, H_{in} , and wave period, T. The input wave heights ranged from 0.1 to 0.4 m, which corresponds to a range of 0.6 m (2.0 ft) $< H_{in} <$

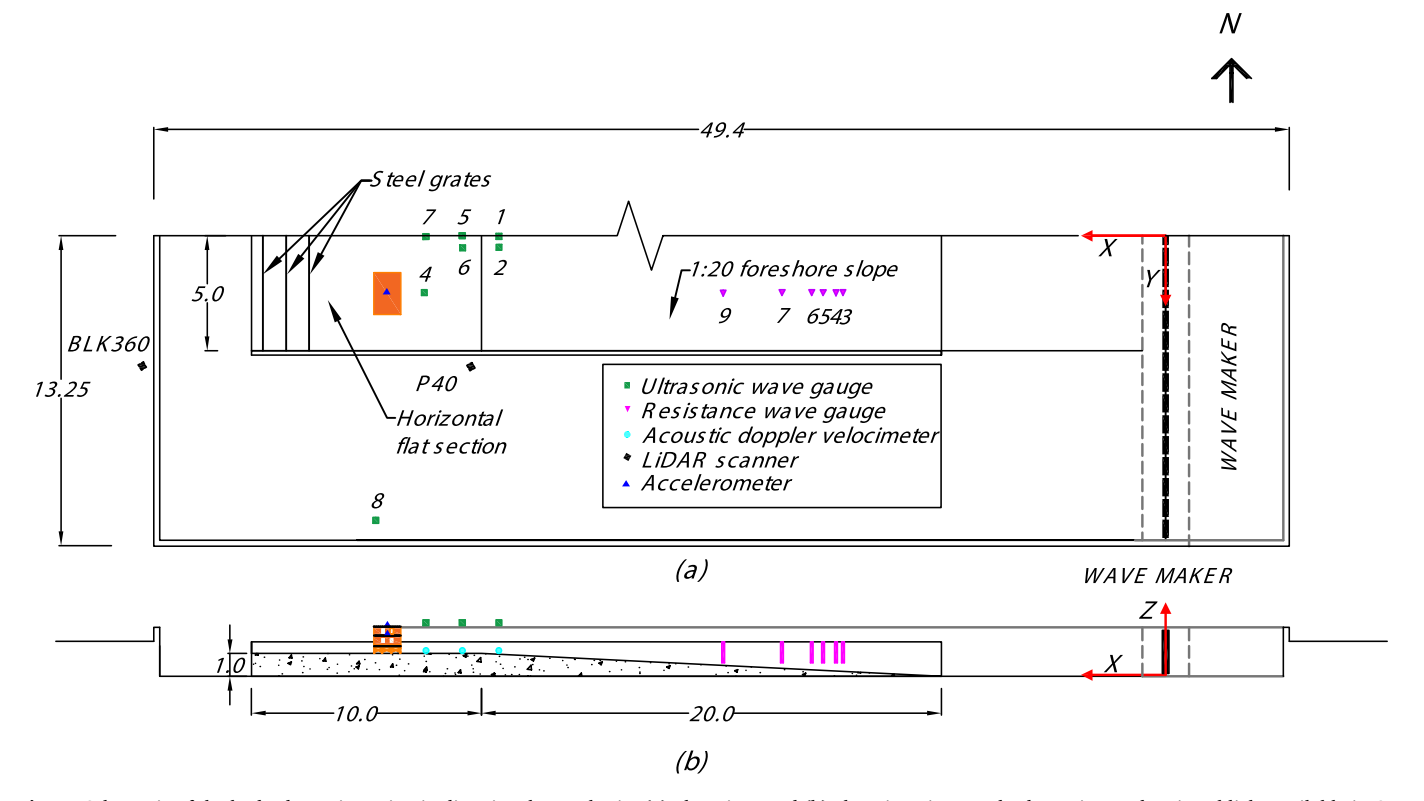


Fig. 5. Schematic of the hydrodynamic testing in directional wave basin: (a) plan view, and (b) elevation view. Hydrodynamic test data is publicly available in Cox et al. [20] and structural testing and system identification data is available in Barbosa et al. [9]. All dimensions are in meters.

Table 1
Summary of wave conditions used in the hydrodynamic testing.

Trial	<i>h</i> ₀ (m)	h (m)	a (m)	H_{in} (m)	T (s)	Wave type at specimen	N_{WE}	Notes
1	1.10	0.10	0.25	0.1	4.5	Broken	_	Scan before Trial 1
2	1.10	0.10	0.25	0.4	4.5	Broken	-	Scan after Trial 2
3	1.12	0.12	0.23	0.1	4.5	Breaking	-	
4	1.20	0.20	0.15	0.2	4.5	Broken	-	
5	1.20	0.20	0.15	0.3	4.5	Broken	-	Scan after Trial 5
6	1.30	0.30	0.05	0.1	4.5	Nonbreaking	40	
7	1.30	0.30	0.05	0.2	4.5	Breaking	80	
8	1.30	0.30	0.05	0.3	4.5	Broken	121	
9	1.30	0.30	0.05	0.3	3.5	Broken	174	
10	1.30	0.30	0.05	0.3	5.5	Broken	208	Scan after Trial 10
11	1.35	0.35	0.00	0.1	4.5	Nonbreaking	248	
12	1.35	0.35	0.00	0.2	4.5	Breaking	289	
13	1.35	0.35	0.00	0.3	4.5	Broken	330	
14	1.35	0.35	0.00	0.4	4.5	Broken	371	Scan after Trial 14
15	1.40	0.40	-0.05	0.1	4.5	Nonbreaking	412	
16	1.40	0.40	-0.05	0.2	4.5	Breaking	453	
17	1.40	0.40	-0.05	0.3	4.5	Breaking	494	
18	1.40	0.40	-0.05	0.4	4.5	Broken	535	Scan after Trial 18
19	1.45	0.45	-0.10	0.1	4.5	Nonbreaking	576	
20	1.45	0.45	-0.10	0.2	4.5	Breaking	617	
21	1.45	0.45	-0.10	0.3	4.5	Breaking	620	Elevated specimen fa

Legend: h_0 = water depth at the wavemaker; h = water depth at the specimen; a, air gap, defined as the elevation of the bottom of the lowest horizontal structural member relative to the still water level; N_{WE} = cumulative number of waves that interacted with the specimen; H_{in} = wave height at the wavemaker; T = wave period. The "Notes" provides information on when the laser scanning was performed and when the specimen collapsed.

2.4 m (7.8 ft) in prototype scale, similar to large storm waves produced by Hurricane Sandy at Ortley Beach, New Jersey [12].

2.2.4. Test Specimen: In-water damage quantification

Laser scans were performed before Trial-1 and before increasing each water level, as indicated on the rightmost column in Table 1, to quantify the damage of the test specimen under successive and more severe surge and wave conditions. Scans were performed using a Leica Geosystems P40 scanner and a Leica BLK360 scanner, which were positioned at the locations shown in Fig. 5. The generated point cloud data were used to quantify the damage sustained by the test specimen [75]. For this purpose, the initial wall sheathing area of the test specimen was determined from the point cloud data obtained before the hydrodynamic testing and compared to the remaining wall sheathing area following each successive scan as the water level was increased.

2.3. Numerical methods

2.3.1. System identification (SID)

For the out-of-water forced vibration testing, two output-only operational modal analysis (OMA) methods were used to identify the natural frequencies, damping ratios, and mode shapes. The OMA methods used were the Enhanced Frequency Domain Decomposition (EFDD)[14]and the Stochastic Subspace Identification (SSI)[13]. Acceleration data collected in the testing were analyzed to extract the modal features, following a similar approach used in Magalhães et al. [40] and Moaveni et al. [45] using the Artemis software [5]. Before applying the EFDD and SSI methods, however, the collected data were post-processed using power spectral densities (PSDs), taken on 1-min windows using the pwelch function from MATLAB's signal processing toolbox [42] to check for high noise signals and corrupted data. A set of post-processing schemes were defined to focus on different sections of the frequency spectrum of interest, similar to what was performed in Mugabo et al. [48]. An upper limit of 40 Hz was considered adequate for capturing the first few natural frequencies of interest and various Butterworth filter windows were used to focus on different sections of the spectrum of interest. To extract modal features in this frequency range, a harmonic peak reduction algorithm integrated in ARTeMIS based on the SSI process orthogonal projection was used [29].

For the in-water hydrodynamic tests and for the FE model results

subjected to the hydrodynamic force time series obtained from the computational fluid dynamic (CFD) modeling in OlaFlow[32], described in Section 2.3.2, PSDs of acceleration response of the specimen were obtained using the *pspectrum* and *plomb* functions available in MATLAB's signal processing toolbox [42]. Hydrodynamic force time series obtained from OlaFlow simulations utilize an adaptive time step for convergence, which resulted in force time series with a non-uniform time step. The MATLAB *plomb* function allowed computing PSDs for monotonically increasing time series with non-uniform time steps. For the *pspectrum* function used, a frequency resolution of 0.5 Hz was utilized.

2.3.2. Computational fluid dynamics (CFD) simulation of pressure distribution

Horizontal pressures on the test specimen in the EW direction were not measured during the hydrodynamic testing. As a result, the pressure time series were obtained through numerical simulation. The CFD hydrodynamic modeling was performed using OlaFlow[32]. OlaFlow is an open-source code, implemented on the OpenFOAM framework and specialized for wave boundary conditions such as piston and flap-type wave maker with active absorption. OlaFlow solves the threedimensional Reynolds averaged Navier-Stokes equation accounting for two phases (water and air) using the finite volume method. The CFD hydrodynamic modeling consists of two components: (1) a numerical wave flume created using the "blockMesh" tool, defining vertices, faces, and boundaries manually, and (2) a specimen created using the "snappyHexMesh" tool, utilizing STL (STereo Lithography) files for geometric data [36]. The numerical wave flume employs varying mesh sizes, ranging from 10 cm to 0.8 cm to minimize computation times, while the specimen utilizes a uniform size of mesh, approximately 0.8 cm for accuracy of the model.

In Fig. 6a, the specimen's mesh configuration is shown integrated into the numerical wave flume. The bottom of each column in the specimen is placed over the flat section of the wave flume, leading to the merging of the two mesh grids. This merging results in a relatively finer mesh, approximately 0.5 cm, at the bottom of each column. The total number of mesh elements is 5 million, and the test specimen is modeled as a rigid body. Fig. 6b shows the locations on the front face of the test specimen OlaFlow model where virtual sensors were located to obtain pressure time series results. The numerical model validations were

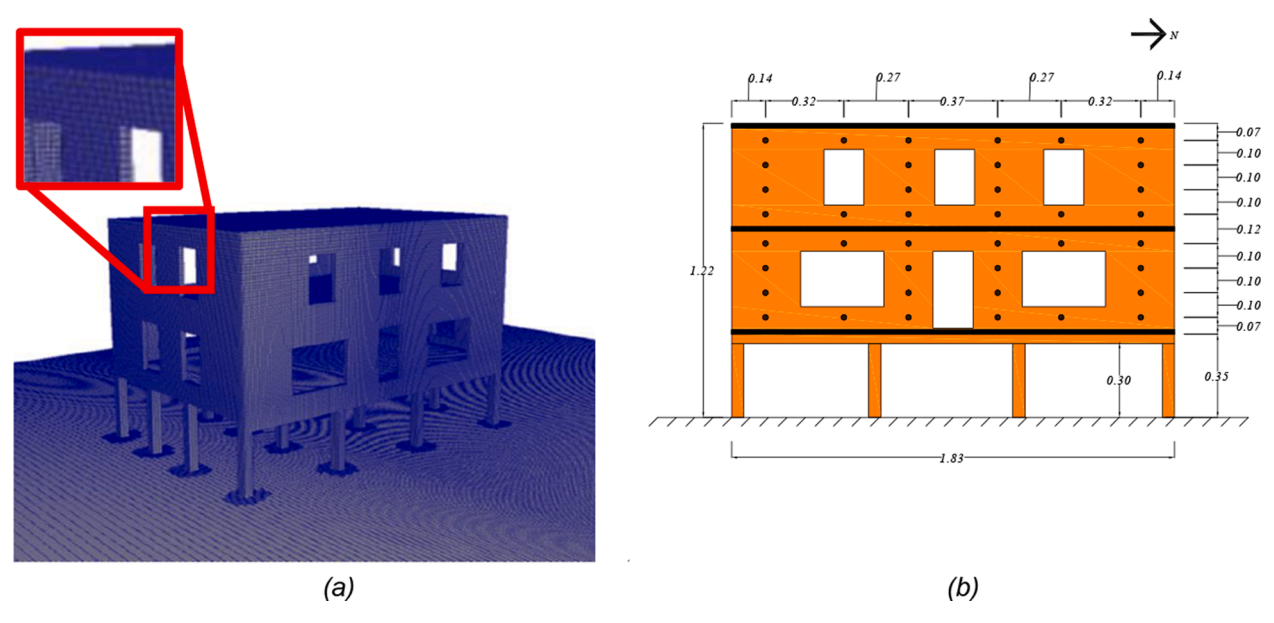


Fig. 6. OlaFlow CFD model used to simulate pressures for the various trials of hydrodynamic tests: (a) specimen mesh setup, and (b) locations for which pressures were recorded on the front face (East face). All dimensions are in meters.

performed through comparisons of experimental vertical pressure measured at the bottom face of the specimen, water surface elevations, and horizontal and vertical velocities near the specimen. The simulation results showed excellent agreement with the experimental measurements and were used to obtain spatial pressure distribution at the front face of the specimen Additional validation information is available in Lee et al. [36].

2.3.3. Finite element modeling and model updating of the test specimen

A series of two-dimensional (2D) linear elastic finite element (FE) models of the test specimen were developed in OpenSees [43]. The FE models capture the behavior of the structural walls in the flow direction using diagonal truss elements to simulate the contribution of in-plane walls to the lateral stiffness of the test specimen. The contribution of out-of-plane shear walls were modeled using elastic beam-column elements. Moreover, the plywood floor and roof of the test specimen were modeled as rigid diaphragms using elastic beam-column elements with modulus of elasticity of 8.6 GPa (1247 ksi). In addition, masses were lumped at two-end nodes at the floor levels. A total mass of 217.5 lb (98.65 kg) was estimated for the test specimen based on the laboratory measurement of the individual component density of 475.70 kg/m³ (29.70 lb/ft^3) , 554.90 kg/m³ (34.64 lb/ft^3) , and 571.90 kg/m³ (35.70 lb/ft^3) lb/ft³) for plywood sheathing, plywood floor slabs, and studs, respectively. Floor level masses of 40.7 kg (89.7 lb), 30.8 kg (68.0 lb), and 27.0 kg (59.6 lb) were estimated for Level-2, Level-3, and roof, respectively. Additionally, the FEM was considered fixed at the lowest horizontal structural member (LHSM) level and hence the piles were not modeled explicitly.

A multi-phased approach was used to update the FE models to simulate observed experimental damage progression, which in part follows the modeling approach and lessons learned in Mugabo et al. [48] during the dynamic characterization and FE model updating of a four-story mass timber building tested under ambient vibration as well as an experimental program described in Mugabo et al. [49].

2.3.3.1. Out-of-water FE models. Fig. 7 illustrates the OpenSees FE model updating approach adopted in this study. With respect to the EW direction, in phase-1, the main lateral force-resisting shear walls were modeled including the exterior light-frame wood shear walls and the plywood diaphragms. The structural properties of the truss elements were simulated based on the quasi-static lateral load-deformation test

results obtained using methods described in section 2.2.1. In phase-2, the interior light-frame wood shear walls were added to the FE model.

The exterior light-frame wood shear walls included in phase-1 were modeled using a pair of equivalent diagonal truss elements in OpenSees. The CUREE model presented in Folz & Filiatrault [25], also widely known as the SAWS model in OpenSees, is used to model the light-frame wood shear walls. The model is based on the behavior of three structural components under quasi-static loading: rigid framing members, linear elastic sheathing panels, and nonlinear sheathing to framing connectors. Fig. 8a shows the hysteretic force-deformation response and Eqn. (1) represents the backbone curve of the CUREE model [25] that is based on the exponential envelope of the 10 model parameters: K_0 the initial stiffness, F_0 the force intercept of the asymptotic stiffness at ultimate strength, F_i the zero-displacement load intercept, δ_u the displacement at ultimate load, r_1 the asymptotic stiffness ratio under monotonic load, r_2 the post-capping strength stiffness ratio under monotonic load, r_3 unloading stiffness ratio, r_4 the reloading pinched stiffness ratio, α the hysteretic parameter for stiffness degradation, β the hysteretic parameter for stiffness degradation.

$$F = \begin{cases} sgn(\delta)(F_0 + r_1 K_0 |\delta|) \left[1 - exp\left(\frac{-K_0 |\delta|}{F_0}\right) \right] : |\delta| \le |\delta_u| \\ sgn(\delta)F_u + r_2 K_0 [\delta - sgn(\delta)\delta_u] : |\delta_u| \langle |\delta| \le |\delta_F| \\ 0 : |\delta| \rangle |\delta_F| \end{cases}$$
(1)

with sgn(.) = the signum function. The quasi-static lateral load-deformation results of the 12 TWs were used to calibrate the five parameters (K_0 , F_0 , δ_u , r_1 , r_2) of the CUREE model. The exponential envelope curve, defined in Eqn. (1), was used in the calibration process. A set of MATLAB scripts was developed to identify the five parameters through an iterative optimization process involving solving a set of constrained least square problems to minimize the difference between the experimental and numerical load-deformation curves. The process involves setting up lower and upper-bound model parameters and a set of initial parameters within these bounds to identify the optimized set of model parameters.

As the objective of the study is the system identification of the elevated light-frame wood shear wall buildings, emphasis was placed to find out the best possible match of the initial stiffness K_0 with the experimental stiffness. This was achieved through a sensitivity study

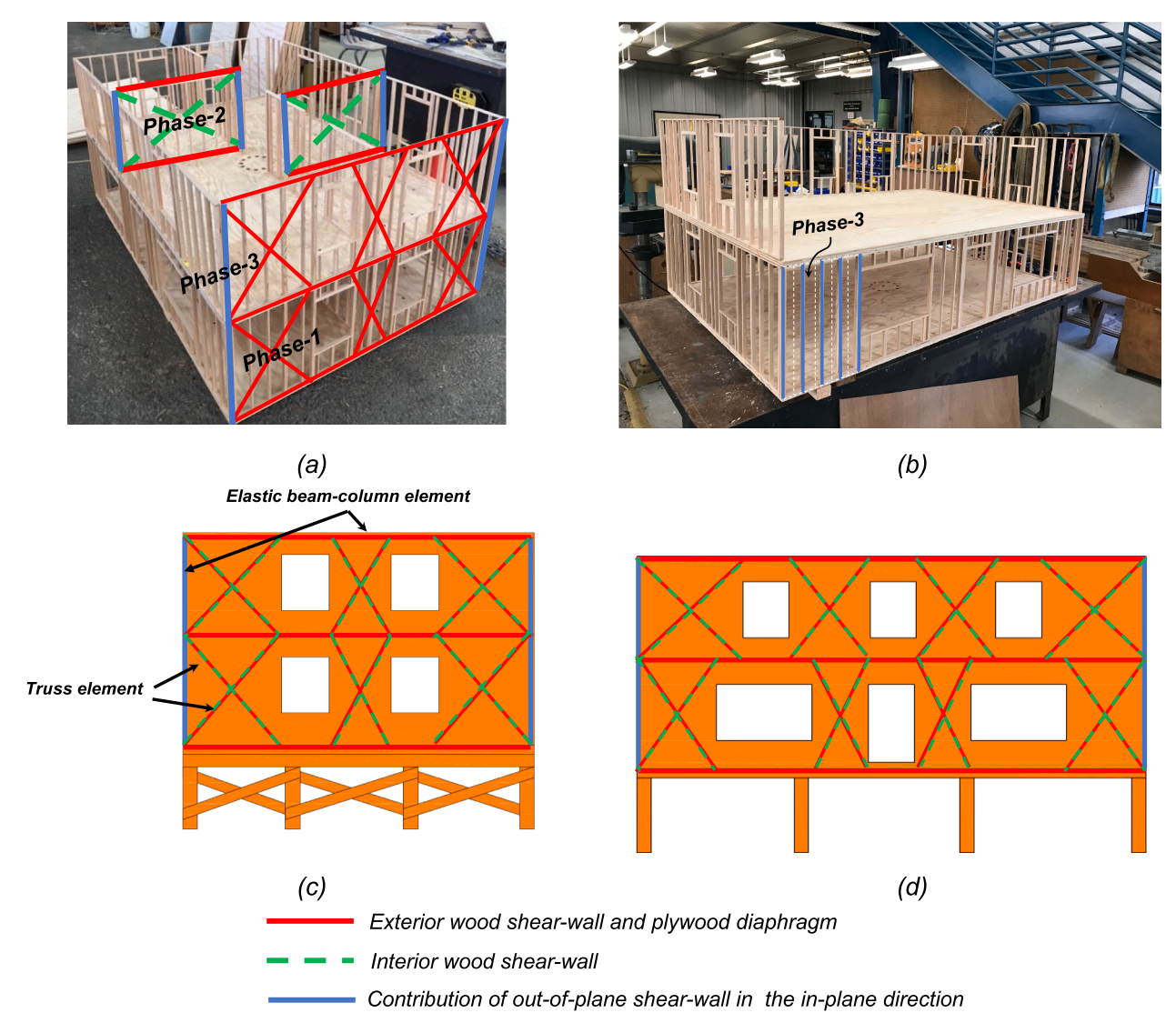


Fig. 7. Multi-phase finite element model development approach for the light-frame wood shear wall building: (a) elements modeled at different phases, Phase-1: In-plane exterior light-frame wood shear wall and plywood diaphragm, Phase-2: Phase-1 + interior light-frame shear wall, Phase-3: Phase-2 + contribution from the out-of-plane light-frame wood shear wall; (b) illustration of Phase-3: out-of-plane contribution; (c) and (d) show the different elements used in OpenSees to model Phase-1 to Phase-3 in the NS and EW directions, respectively.

involving calibrating K_0 to three different force levels that are some fractions of the peak force F_u ranging (0.01–0.2) F_{tb} (0.05–0.1) F_{tb} and (0.05-0.2) F_{u} . Fig. 8b shows the coefficient of variation (COV) of model parameters obtained through the calibration process using the 12 TWs load-deformation data. Based on the calibration results, the (0.01-0.2) F_{ij} case resulted in the lowest COV for K_0 . Fig. 8c and Fig. 8d show the load-deformation envelope of fitted models obtained through calibration for TW-01 and TW-06, respectively. Even though the initial stiffness was well simulated for both TW cases shown in the figure, the calibration process resulted in better agreement between the load-deformation experimental and numerical response curves for TW-06 compared to that of TW-01. Moreover, the overall goodness-of-fit of calibrated model parameters was estimated using mean R^2 value, which represent the discrepancies of the fitted load-deformation to that of experimental load-deformation of all the panels. The mean R^2 value for the K_0 : $(0.01-0.2) F_{tv} K_0$: $(0.05-0.1) F_{tv}$ and K_0 : $(0.05-0.2) F_{tt}$ cases were found to be 0.91, 0.87, and 0.89, respectively. Based on the mean R^2 value, model parameters corresponding to K_0 : (0.01–0.2) F_u case were selected for modeling the shear walls using truss elements.

The five cyclic response parameters (F_i , r_3 , r_4 , α , and β) of the CUREE model are not obtainable from the quasi-static lateral load-deformation

tests since these require cyclic test data. Here, these parameters were obtained following the recommendations presented in ATC [8] for modeling wood shear wall systems. Table 2 lists the 10 model parameters used for exterior and interior light-frame wood shear walls in phase-1 and phase-2, respectively.

In phase-3, the out-of-plane contribution from the light-frame wood shear wall in the NS direction to the stiffness in the EW direction was modeled using elastic beam-column elements. An equivalent transformed cross-section of the elastic beam-column element was estimated by transforming plywood sheathing to an equivalent stud-only cross section. A modulus of elasticity of 12.44 GPa (1790 ksi) was assigned considering Douglas-fir studs [72]. The contribution of the out-of-plane shear walls was adjusted through calibration using SID results obtained from the out-of-water forced vibration tests described in section 2.2.2, using methods described in section 2.3.1.

A correlation phase, phase-4, was added to adjust the modeling parameters of different phases to obtain a better correlation of the FE model results with that of out-of-water dynamic structural characterization experimental results. This correlation phase accounts for inaccurate estimation of masses and their distribution, as well as uncertainty in lateral stiffness contributions from different components, such as

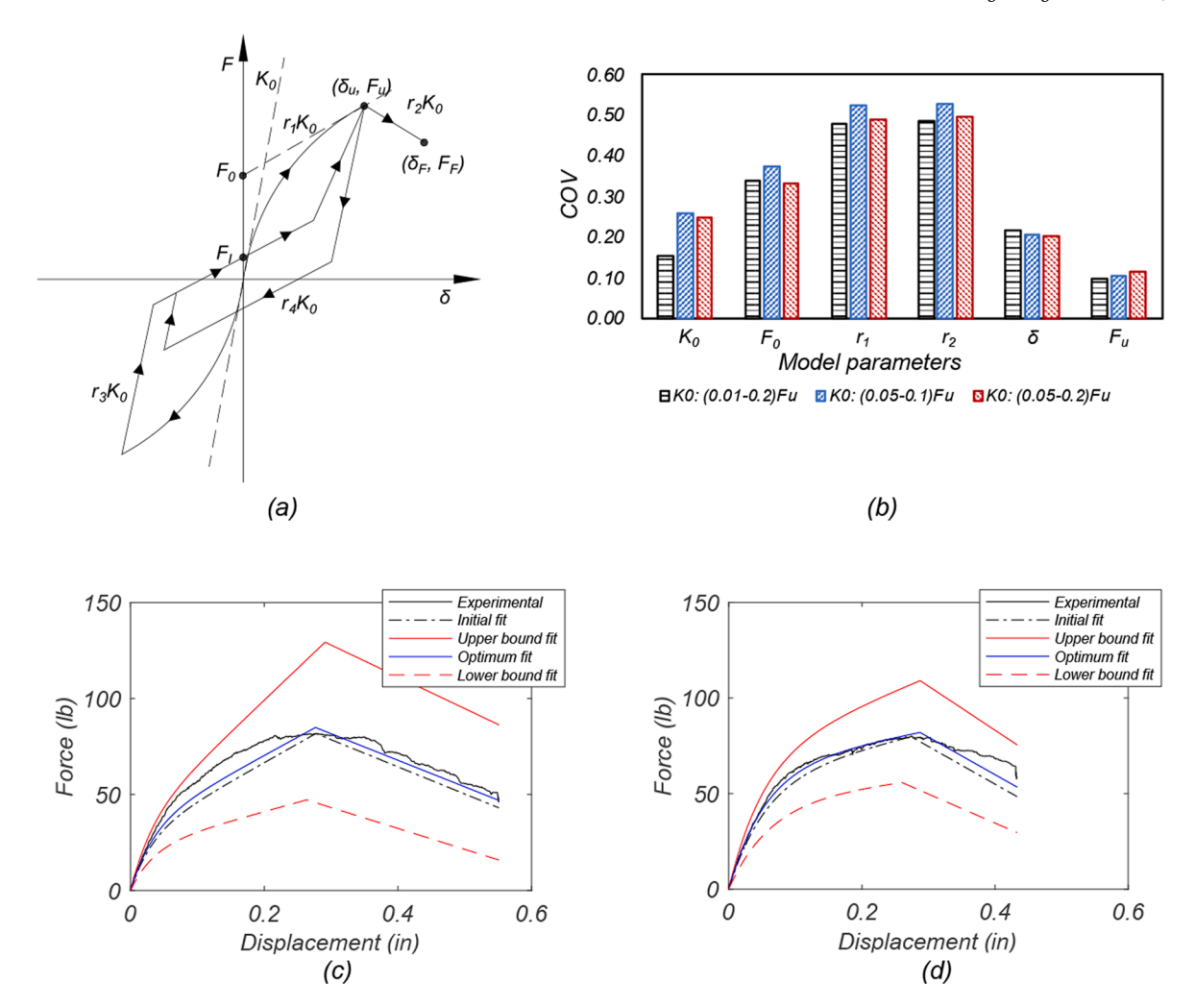


Fig. 8. CUREE model calibration based on test walls (TWs) static load-deformation data: (a) load-deformation curve for CUREE model, (b) model parameter sensitivity based on initial stiffness fitted to test wall data and fitted CUREE model to (c) TW-01 and (d) TW-06.

Table 2CUREE model parameters for the exterior and interior light-frame wood shear wall used in Phase-1 and Phase-2 of OpenSees FEM.

	K_0 (kN/mm/m)	F ₀ (kN/mm)	r_1	r_2	δ_u (mm)	F _I (kN/mm)	r_3	r ₄	α	β
Exterior frame	0.495	0.00049	0.13	-0.20	0.51	$0.1 \; F_0$	1.00	0.015	0.85	1.10
Interior frame	0.124	0.00049	0.13	-0.20	0.51	$0.1~F_0$	1.00	0.015	0.85	1.10

actual sheathing thickness and nailing (which could not be appropriately scaled to a 1:6 scale), floor joist contributions, as well as the effect of added paints, all of which were not considered in earlier phases.

2.3.3.2. In-water FE modeling. For the in-water hydrodynamic conditions, force time series, obtained from pressure simulation in the Ola-Flow CDF model, were applied at floor levels to the OpenSees FE models developed. The Phase-4 FE model described in section 2.3.3.1 was used for modeling in-water cases while no damage was observed. Following each trial where notable damage was observed, the FE models were modified (phase-5 of FE model updating) to match the SID results obtained from the in-water hydrodynamic tests described in section 2.2.3 using the methods described in section 2.3.1.

In phase-5, the FE model calibration included a reduction in stiffness due to quantified damage due to the multi-wave multi-trial overland flow hydrodynamic experiment. The observed damage included vertical

stud damage as well as sheathing wall loss in both the NS and EW directions. The FE model was modified by adjusting the stiffness of the first-story exterior light-frame walls (phase-1) and out-of-plane shear walls (phase-3) by removing elements commensurate with the damage observed during hydrodynamic testing and quantified based on the analysis of the laser scan point cloud data in Yu et al. [75].

2.3.3.3. Additional FE modeling considerations. In the dynamic analyses performed, the Newmark constant acceleration method was employed in OpenSees to perform response history analyses under wave action. The Newton algorithm was used to solve the linear system of dynamic equilibrium equations at each time step. To improve convergence rates, an iterative scheme composing of a reduction in time step, change in solution algorithm, or slightly increasing the tolerance criteria was implemented in OpenSees. Rayleigh damping proportional to mass and current stiffness was assigned at 6.6% equivalent damping at the

fundamental period $T_I = 0.046$ s and at a period of 0.016 s, corresponding to more than 90% of mass participation of the FE models. The value of 6.6% equivalent damping used herein was based on the damping computed from the free vibration tests performed on the test specimen [23].

Lastly, due to inherent uncertainties associated with modeling (e.g., [41,45]), a sensitivity analysis of the response to the main modeling parameters was performed as part of the validation of the FE model developed, including the sensitivity of the response to damping modeling. Chopra [17] recommends damping ratio values for different types of structures for two levels of motion: working stress levels (corresponding to stress levels no more than one-half the yield point) and stress at or just below the yield point based on the data collected from instrumented buildings during seismic events. For use in the elastic analysis of wood structures with nailed joints, Chopra [17] recommends the use of damping ratios of 5–7% and 15–20% for working stress level and at or just below yield-point, respectively. In this study, three levels of damping ratios of 6.6% (obtained in free vibration tests as discussed below), 15%, and 20% (as per the recommendation of [17]) are used.

The combined CFD finite volume modeling (Section 2.3.2) and multiphase FE model updating (Section 2.3.3) adopted herein have several practical aspects. Firstly, without experimental horizontal pressure data, it allowed simulating of the horizontal pressure on the test specimen in the flow direction through a validated OlaFlow CFD model of the hydrodynamic experiment. Secondly, the simulated pressure is then used as loading input in the multi-phase FE model updating of the test specimen, which allowed for identifying the contribution and sensitivity of different structural components and their properties on the SID of the test specimen and studying damage progression correlation between the experimental and FE model data in a step-by-step manner.

3. Results and discussion

3.1. Experimental system identification of the test specimen

3.1.1. Out-of-water system identification

For the ambient vibration (AV) and other out-of-water forced vibration tests, Table 3 shows the natural frequencies and damping ratios results, obtained using the EEFD and SSI OMA methods. The mode shapes are not shown herein in the interest of brevity. The four different excitation functions were applied at different levels of amplitude. To assess the acceleration amplitudes, a root mean square (RMS) function was applied to Level-2 acceleration data. The resulting acceleration RMS for the AV, WN, Ramp, and Ramp Ecc. functions were $2.31\times 10^{-4}~\rm g, 9.18\times 10^{-2}~\rm g, 5.62\times 10^{-2}~\rm g, 5.98\times 10^{-2}~\rm g, respectively.$ To evaluate the amplitudes of excitation experienced by the structure, Fourier Amplitude Spectra (FAS) were developed for the EW (parallel-to-wave) direction accelerations at the Level-2 for the WN, AV, Ramp, Ramp Ecc.

Table 3Summary of natural frequencies and damping in the NS and EW directions identified using different methods.

OMA Method	Mode Main Direction	Identified Parameters	AV	WN	Ramp	Ramp Ecc.
EFDD	NS	f (Hz)	15.7	15.4	15.1	15.4
		ζ (%)	8.0	2.3	3.0	2.7
	EW	f(Hz)	23.0	22.1	19.3	18.6
		ζ (%)	4.7	7.0	10.2	6.4
SSI	NS	f (Hz)	16.0	15.6	_	15.4
		ζ (%)	7.8	5.2	_	1.8
	EW	f(Hz)	23.0	21.5	19.4	18.8
		ζ (%)	5.2	6.2	7.2	2.9

Legend: **EFDD** – enhanced frequency domain decomposition; **SSI** – stochastic subspace identification; f – frequency; ζ – damping ratio; AV – ambient vibration excitation; WN – white noise excitation; Ramp – concentrically applied ramp function excitation; Ramp Ecc. – eccentrically applied ramp function excitation.

datasets. The same data duration (approximately 2 min) was used for all four excitation methods to obtain a comparable frequency amplitude amongst the four excitation methods used. The acceleration data were filtered using a Butterworth filter of order n=3 and banded between 0.5 and 30 Hz, thus focusing on the frequency range of interest for the specimen's first modes of vibration. For this frequency range of interest, it was observed that the Ramp and Ramp Ecc. resulted in amplitudes that were approximately 0.6 and 250 times the amplitude obtained for the WN and AV Level-2 accelerations FAS results, respectively, consistent with the magnitude of the RMS acceleration values of different excitation functions.

From Table 3, the mode in EW had a higher natural frequency, indicating a stiffer lateral system, which is in agreement with the use of braced foundation piles in the EW direction and the absence of bracing in the NS direction. In addition, the natural frequencies varied with increasing excitation levels from ambient vibration to ramp function. The variation in natural frequencies is most noticeable for the EW mode, which is the direction in which the shakers excited the structure (see L1 and L2 in Fig. 4). The natural frequency in the EW direction ranged from 23.0 Hz for the AV method to 19.4 Hz for the Ramp method. The natural frequency was further reduced to 18.8 Hz when the Ramp function was applied eccentrically in the EW direction. There is less variation in the NS direction natural frequencies, with frequency ranging between 16.0 Hz for AV to 15.4 Hz for the Ramp Ecc. function. This can be explained by the driven excitations (WN, Ramp, Ramp Ecc.) being applied in the EW direction, and not in the NS direction. A torsional mode was identified when the eccentric ramp function was applied to the structure. The fundamental torsional mode had a natural frequency of 37.4 Hz and a damping ratio of 4.1 %, however since the torsional mode was not consistently identified with the other excitation functions, it was not listed in Table 3.

3.1.2. In-water system identification

Roof acceleration data gathered in hydrodynamic tests are used herein for in-water system identification of the test specimen in the EW direction. Fig. 9 shows the roof acceleration time series and PSDs obtained for Trail-6 and Trial-19 as examples. As can be seen in Fig. 9a and Fig. 9b, Trial-19 produced a consistently higher roof acceleration response compared to Trial-6, which can be attributed to the higher inundation depth of the former compared to the later. Note that for the PSD analysis, acceleration time series were divided into four segments, each represented with distinct colors. Fig. 9c and Fig. 9d show the PSDs of roof acceleration response for Trial-6 and Trial-19, respectively. The natural frequencies obtained, which correspond to peak values of PSDs of each roof acceleration series segment, for Trial-6 (ranging between 23.2 and 23.8 Hz) are consistently higher than those obtained for Trial-19 (ranging between 17.4 and 18.1 Hz), indicating a decrease in natural frequencies with an increase in observed damage.

The reduction in natural frequencies as a function of the increase in trial number is further explored in Fig. 10 for Trial-6, Trial-7, Trial-8, Trial-16, and Trial-19. For each trial, four natural frequencies are reported, which correspond to those obtained for each of the four acceleration segments described before. Moreover, the percentage sheathing loss observed at each trial is also reported. The reduction in natural frequency with trial number can be attributed in part to the accumulated loss of sheathing. The natural frequency reduction can also partly be attributed to the loosening of nails and other connections and other load duration effects on wood members and connections [60].

3.2. Experimental to numerical model SID correlation study

3.2.1. Out-of-water experimental to numerical model SID correlation

Fig. 11 shows the natural frequencies of OpenSees FE models (phase-1 to phase-4) with respect to the natural frequencies of the test specimen obtained in the free vibration pluck tests, which were 21.67 Hz and 15.2 Hz in the EW and NS directions, respectively. The FE model natural

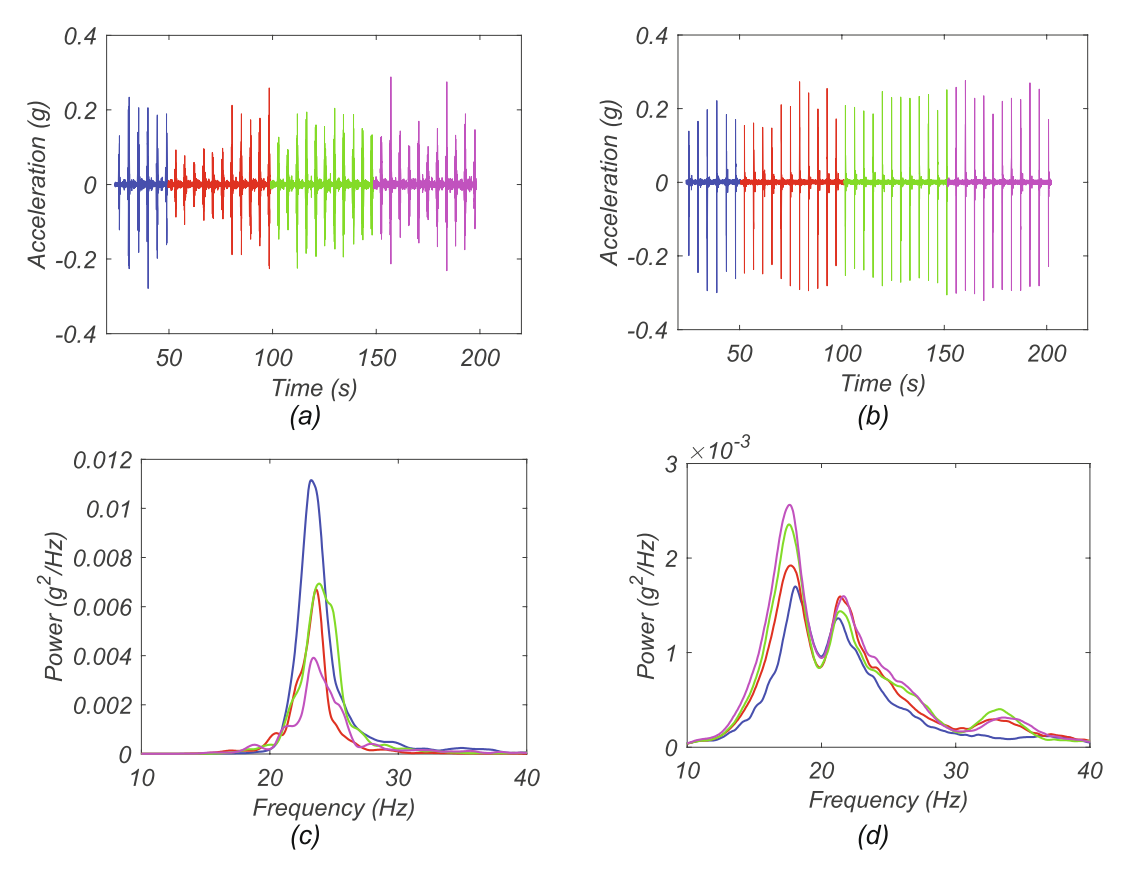


Fig. 9. Test specimen in-water hydrodynamic response in terms of roof acceleration time series for (a) Trial-6 and (b) Trial-19. Corresponding PSDs for (c) Trial-6 and (d) Trial-19. Note that approximately first 20 s of time series were not considered in the data analysis reported here and the PSD of a given color correspond to the PSD obtained using acceleration time series segment of corresponding color shown in (a) and (b).

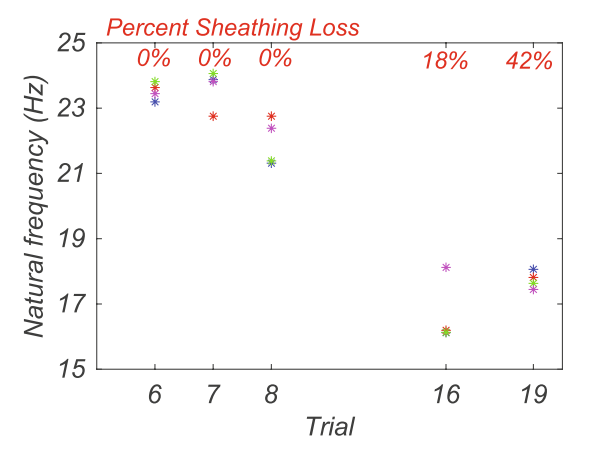


Fig. 10. Test specimen natural frequency as a function of the hydrodynamic test trial number. Frequencies presented as stars with different colors corresponding the colors used in acceleration time series for each trial shown in **Fig. 9.** In red, the percentage sheathing loss per trial is indicated at the top of the plot.

frequencies are normalized with respect to the respective average free-vibration natural frequencies obtained in the free vibration tests. The natural frequencies computed for phase-1 were significantly lower than those observed in free vibration testing corresponding to 16% and 33% of the experimental natural frequencies in the EW and NS directions, respectively. The addition of interior frames in phase-2 resulted in only a slight increase in the estimated natural frequencies for both directions. The addition of the out-of-plane contribution of wood-frame shear walls to in-plane response in phase-3 resulted in a large increase in natural

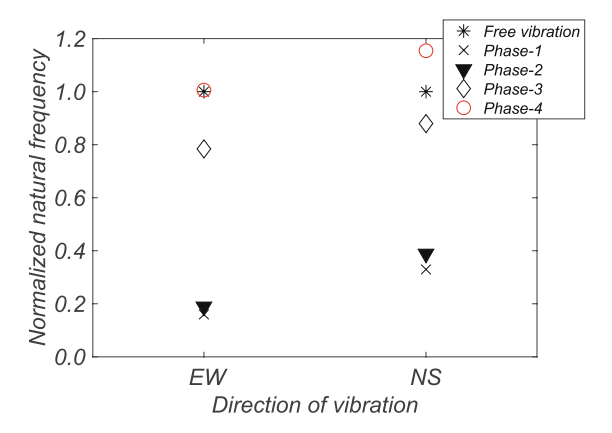


Fig. 11. Phase-1 to phase-4 FE model EW and NS fundamental frequencies normalized to free vibration frequencies in the respective directions.

frequencies in both directions, reaching 79% and 88% of free vibration frequencies in the EW and NS directions, respectively. In phase-4, an increase in the stiffness of interior and exterior walls coupled with an increase in the out-plane stiffness contribution by a factor of two resulted in good agreement between FE model frequencies and free vibration frequencies yielding normalized natural frequency of 1.01. In the NS direction, a similar correlation effort resulted in lesser agreement (normalized natural frequency of 1.15). A factor of two increase in the stiffness of walls used in the correlation phase is relatively low compared to the approach used in Mugabo et al. [48], where the stiffness of an exterior metal façade and the glazing were increased by a factor of 10.25 and 2.8, respectively to achieve good agreement of FE model natural

frequencies with that of measured natural frequencies.

A tornado sensitivity analysis was performed to identify the relative significance of the FE model parameters on the estimation of the natural frequency of the test specimen in the EW direction. The mass of the test specimen, m, elastic modulus of the plywood slab floor diaphragm, E_{slab} , and lateral stiffness of the light-frame wood shear walls, K_0 , were considered as the variables for the sensitivity study. Fig. 12 lists the statistical parameters and associated probability distribution functions used for these three variables. In addition, a tornado diagram for the normalized natural frequency of the test specimen for varying perturbation of the random variables is also shown in Fig. 12. The vertical line in the middle of the tornado diagram represents the normalized frequency corresponding to the phase-4 FE model with all the parameters set to their median values. The horizontal bars represent the swing of the normalized frequency for different random variables set to their 10th and 90th percentile, one by one, while keeping the rest of the variables to their median values. According to this figure, the mass of the test specimen m is the most significant random variable affecting the natural frequency followed by E_{slab} and K_0 , which is expected since the natural frequencies are proportional to the square root of the ratio of stiffness and mass, but the stiffness is comprised of multiple components, such as K_0 and E_{slab} . This result indicates that it is important that the mass of the specimens tested in fluid-structure interaction experimental programs be measured explicitly. In addition, the importance of the stiffness terms indicates that additional static lateral testing of components is extremely important as scaled specimens are designed and constructed since currently there is a lack of test data that can be used to calibrate the lateral stiffness terms of scaled specimens.

3.2.2. In-water experimental to numerical model SID correlation

Fig. 13a to 13c show pressure simulation locations, pressure distributions at the front face of the specimen at the virtual sensors in the OlaFlow model, and sample pressure time series results obtained from the OlaFlow model for Trial-7. Trial-7 resulted in a breaking wave condition at the test specimen (Table 1), with input wave height at wavemaker of $H_{in} = 0.2$ m and wave period of 4.5 sec, water depth at the specimen location of h = 0.3 m, and air gap of a = 0.05 m. In Fig. 13b, the mean and mean \pm standard deviation of the normalized maximum pressures along the virtual sensors indicated on the shaded region in Fig. 13a. The maximum pressure is normalized with respect to static pressure terms, ρgh , where ρ is the water density (1000 kg/m³), g is the gravitational acceleration (9.81 m/s²), and h is the water depth (m) at the specimen location. Eight (8) waves of Trial-7 were used for computing the mean and mean \pm standard deviation pressure distributions. As can be seen in this figure, maximum mean pressure was observed at the virtual sensor P_1 , located 0.07 m above the lowest horizontal structural members, LHSM). The pressures gradually decreased to zero at 0.72 m above the base of the specimen. In the interest of brevity of this paper, pressure distributions for other trials are

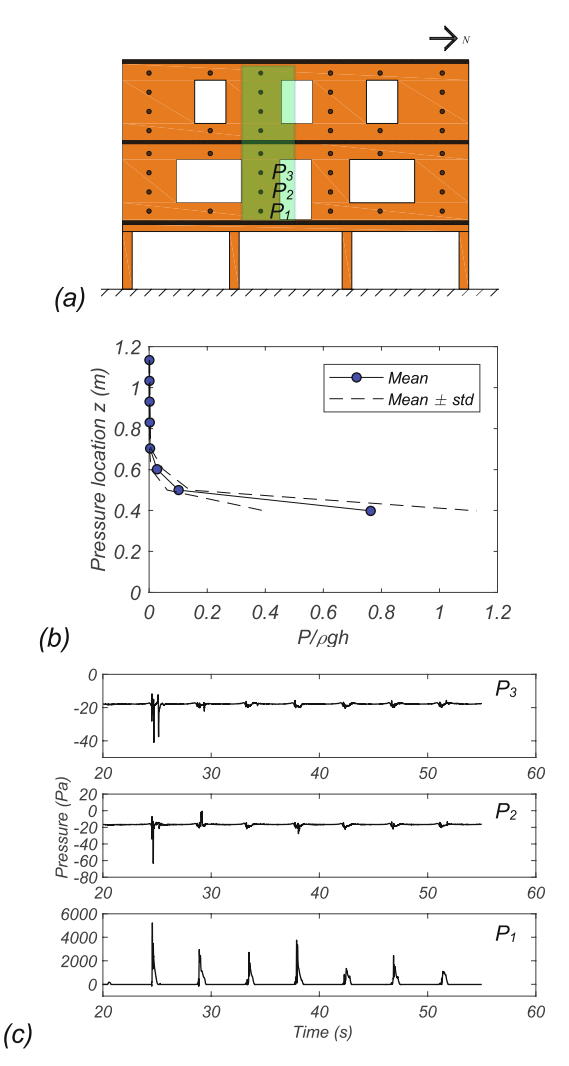
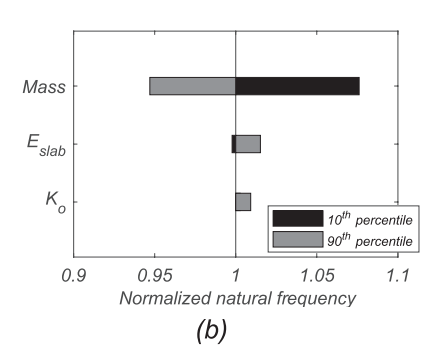


Fig. 13. (a) Virtual pressure sensor locations in the OlaFlow model (black dots) with three labelled sensors; (b) normalized peak pressure distribution along the shaded stripe (Fig. 13a) for Trial-7. Mean and mean+/- standard deviation peak pressures were computed considering the first eight wave cycles of Traial-7. Note, peak pressure values were normalized to static pressure terms, $\rho g h$, where ρ is the water density (1000 kg/m³), g is the gravitational acceleration (9.81 m/s²), and h is the water depth (m); and (c) pressure time series for Trial-7 for three virtual sensors labelled in Fig. 13a.

Random variable	Statistical parameter	Distribution	Reference	
m (kg)	μ = 98.65, COV = 10%	Normal	JCSS (2006)	
E _{slab} (MPa)	μ = 8.60, COV = 13%	Lognormal	JCSS (2006)	
K ₀ (kN/mm/m)	μ = 0.495, COV = 15%	Lognormal	This study	



(a)

Fig. 12. FE model natural frequency parameter sensitivity in the EW direction: (a) variables, distribution, parameters used; and (b) tornado diagram presenting the swing in normalized natural frequency for 10th and 90th percentile perturbations for mass, m, modulus of elasticity of slab E_{slab} , in-plane shear wall stiffness, K_0 . Note: JCSS [34].

not presented herein although additional ones can be found in Lee et al. [36].

Fig. 14a shows the correlation between experimental and phase-4 FE model acceleration time history results at roof level for Trial-7. Note that the phase-4 FE model was used here since no damage was observed for Trial-7. Though discrepancies in magnitudes of the accelerations can be observed qualitatively, the time series are well correlated. The experimental peak roof accelerations were found to be 0.43 g, which is about 17% lower than the FEM peak absolute roof acceleration of 0.49 g. Over the whole simulated duration, the percentage difference between experimental and FEM peak (maximum absolute) roof acceleration results varied between 17.1% and 76.2% for the wave cycles simulated. Fig. 14b shows the PSD as a function of the natural frequency. Herein, the first 18 s of the acceleration time history during which no wave impacted the structure were used in the computation of the PSDs. This time window was chosen to represent the still water condition around the test specimen prior to experiencing any wave. Overall, the PSDs for the experimental and FE model results agree reasonably well in terms of natural frequencies and magnitudes. The natural frequencies identified were 24.30 Hz and 22.10 Hz for experimental and FE model simulations, respectively. The FE model frequency is about 9.05% lower compared to the experimental frequency. The discrepancies between experimental and simulation results in Fig. 14 can be attributed to the assumption that the FEM consists of 2D linear elastic elements and due to the uncertainties associated with the damping model, both of which can be further investigated in the future using more advanced 3D nonlinear structural model loosely or tightly coupled with - computational fluid dynamic (CFD) modeling.

PSDs were also computed for different wave cycles of a given trial. Fig. 15 shows the experimental and FE model PSDs for waves 6, 7, and 8 of Trial-7. The natural frequencies identified were 26.80 Hz, 24.10 Hz, and 21.7 Hz for waves 6, 7, and 8, respectively, for experimental data. The corresponding natural frequencies were 22.05 Hz, 21.85 Hz, and 21.05 Hz for the FE model simulation response data. For both the experimental and FE model simulation cases, natural frequencies decrease with an increasing number of wave impacts, consistent with the results shown in Fig. 14, where the identified natural frequencies for the experiment are larger than the ones identified from the FE model results. Moreover, the stiffer responses of the experimental data compared to FE model simulations for these in-water tests are consistent with the system identification results obtained for the out-of-water tests.

3.3. Experimental to numerical model damage progression analysis

For Trial-2, Trial-5, and Trial-10, no damage was identified during testing. Damage was observed and quantified for Trial-14 and Trial-18.

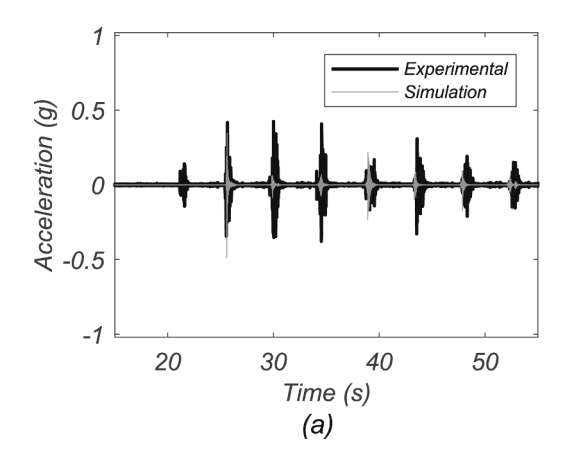
In the EW direction (parallel-to-wave) direction, a loss of the area of sheathing of 0% and 8% relative to the initial state of the building were quantified for Trial-14 and Trial-18, respectively. In the NS (perpendicular-to-wave) direction, a sheathing area loss of 18% and 42% were estimated for Trial-14 and Trial-18, respectively.

Based on the damage quantification, a damage progression correlation analysis was performed using the phase-5 FE model. Fig. 16 shows the damage progression in terms of the degradation of natural frequencies of the test specimen from experimental data and the FE model simulation data. The roof acceleration time histories of Trial-6, Trial-7, Trial-8, Trial-16, and Trial-19 were used for this damage progression analysis. For these five trials, the corresponding loss of area of sheathing was 0%, 0%, 0%, 18%, and 42% in the NS direction, respectively. From Fig. 16a, the degradation of natural frequencies estimated in the FE model simulations are in good agreement with those estimated using the experimental data, even though the simulations resulted in lower medians while no trend was observed in the scatter. The inter-story drift ratios (IDRs) are also estimated from the FE model simulations, but in the interest of brevity and since no displacement results were measured during the testing, these are not validated in this paper.

Fig. 16b shows the comparison of peak roof accelerations for the experimental and FE model simulations as a function of the damping ratio. Damping ratios estimated in this study show large variations for both the directions (NS: 1.8% to 8%; EW:6.6% to 10.2%) depending on the vibration tests and estimation method, similar to what has been observed in the literature (e.g., [45]. For the intact test specimen (0% sheathing area loss) relatively good agreements between experimental and simulated peak floor accelerations are observed for a damping ratio of 6.6% in Trial-6 and Trial-7. However, as damage increased with increasing wave intensity and the number of wave impacts, the FE model simulations with a 6.6% damping ratio failed to capture the experimental peak roof accelerations in Trial-8 and Trial-16. Better agreement between the experimental and FE model results are obtained with the use of higher damping ratios of 15% and 20%, as the specimen likely experienced additional sources of energy dissipation in these trials. Overall, the FE model failed to predict the peak acceleration for the highly damaged specimen in Trial-19. Lastly, Fig. 16b highlights that appropriate damping values should be used commensurate with the loading and resulting stress level experienced by structures, especially when all sources of energy dissipation are not explicitly modeled.

4. Conclusion

Structural system identification (SID) and damage progression of a 1:6 scale elevated light-frame wood shear wall residential building were studied in this paper under increasing hurricane wave and surge over



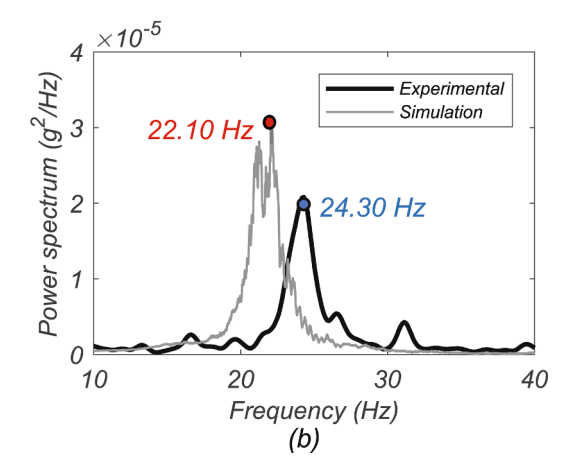
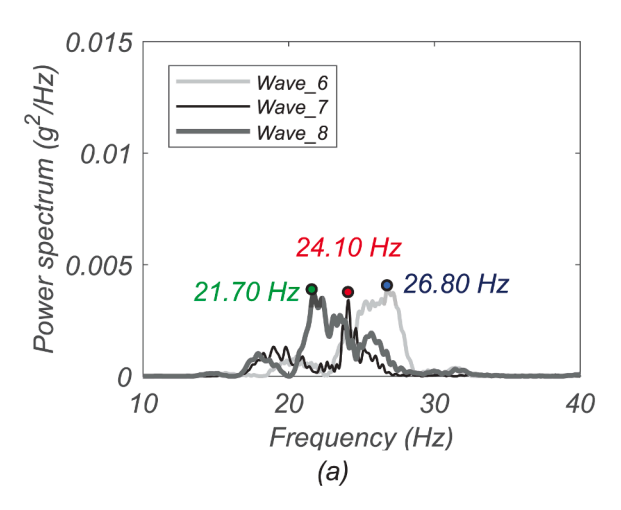


Fig. 14. Experimental and phase-4 FE model results: (a) roof acceleration time histories, and (b) power spectral density of roof level acceleration responses in the EW direction using first 18 s of Trial-7 data.



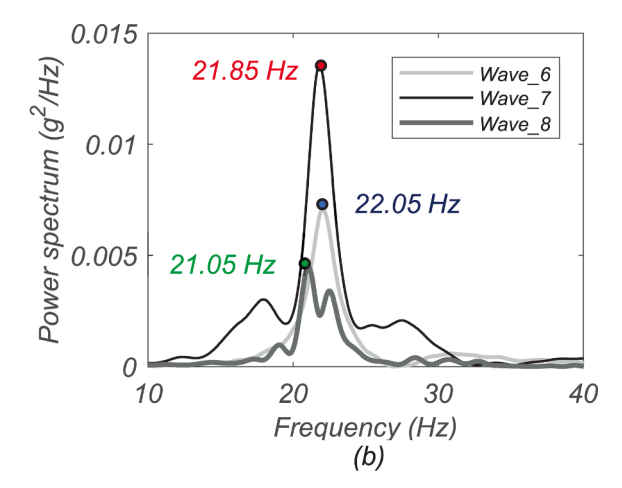


Fig. 15. Natural frequencies in the EW direction for waves 6, 7, and 8 of Trial 7 based on: (a) experimental results, and (b) phase-4 FE model simulation results.

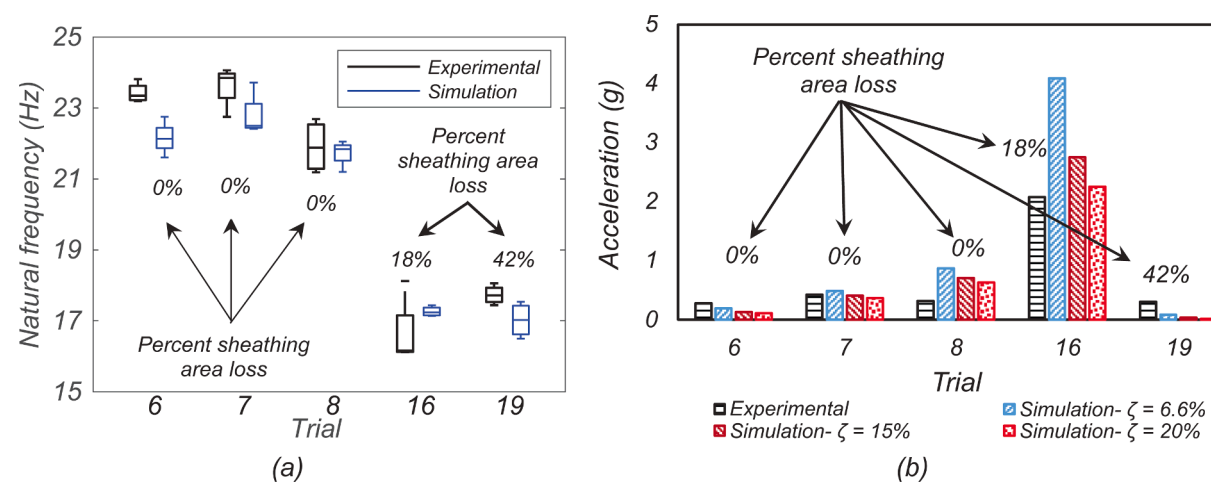


Fig. 16. Damage progression identified in terms of EW fundamental natural frequency and damping ratio: (a) natural frequencies as a function of trial number and damage quantified by the percentage area loss, (b) peak roof accelerations in the EW direction over successive wave trials for different values of simulated Rayleigh damping.

land flow conditions using several experimental and numerical methods. A physical model (referred to in the paper as the test specimen) of an elevated building was developed through careful design to appropriately scale the strength and stiffness of the test specimen compared to a fullscale building prototype. Various static and dynamic experimental methods were used on the test specimen in out-of-water condition (e.g., quasi-static lateral load-deformation testing of components, free vibration, ambient vibration, and forced vibration testing) and in-water condition (destructive hydrodynamic testing) to evaluate the correlation of experimental and FE model simulated SID and damage progression results. Moreover, a multi-phase FE model updating approach was implemented, which included the use of pressure time series results from CFD OlaFlow simulations that were aggregated to force time histories and then were applied to OpenSees FE models. Using calibrated FE models, a sensitivity study was performed to identify the relative contribution of different components to lateral response and to understand the correlation between simulated and experimental SID under increasing hurricane overland surge and wave loading. The main findings of the study are:

1. For the out-of-water tests:

a. The fundamental natural frequencies obtained using different experimental methods, including free vibration, ambient

- vibration, and forced vibration showed that the identified natural frequencies are sensitive to the intensity of the shaking.
- b. The FE models of the test specimen were able to capture the fundamental natural frequencies obtained in out-of-water free-vibration tests for both the EW (parallel-to-wave) and NS (perpendicular-to-wave) directions. Based on the calibration approach used, a better agreement of the ratio of experimental to numerical fundamental frequencies was achieved in the EW (parallel-to-wave) direction (approximately 1% error) compared to the NS (perpendicular-to-wave) direction (approximately 15% error).
- c. Out-of-plane walls and sheathing played an important contribution to lateral stiffness.
- d. Results from the natural frequency tornado sensitivity analysis of the parameters assigned to the FE models indicate that the mass of the test specimen was the most significant variable, followed by elastic modulus assigned to the slab elements. and then lateral (initial) stiffness of the shear walls.

2. For the in-water tests:

a. A correlation study of the experimental and simulated data obtained from the coupled OlaFlow and OpenSees simulations was performed. The fundamental frequencies obtained agreed well with those obtained in the experiment.

- b. The natural frequencies identified decreased with increasing wave intensity and the number of wave impacts for both the experimental and simulation as the test specimen accumulated damage.
- c. The FE model simulations were able to capture the damage progression of the test specimen reasonably well, both in terms of the median estimates and scatter of degradation of natural frequencies when compared to those observed in the destructive hydrodynamic experiment. For each of the trials simulated, the OpenSees results showed lower median natural frequencies compared to those obtained in the hydrodynamic experiment (the ratio of experimental to FE model frequencies varied between 1.03 and 1.22).
- d. The peak floor accelerations estimated using the FE models were found to be sensitive to the level of damping ratio used. It was observed that the use of an appropriate level of damping ratio commensurate with the loading and resulting stress level experienced by the test specimen results in better agreement between experimental and simulated peak floor accelerations.

Mass, stiffness, and damping have all been identified to play a key role in the estimation of the peak responses under hydrodynamic loading. Efforts should be made for better quantification of these quantities in future fluid–structure interaction experimental studies that focus on estimating damage to specimens. In addition, the FE modeling approach implemented in OpenSees can be further used to develop hurricane wave and surge fragility functions of infrastructure in the future. However, adjustments made to linear elastic out-of-plane wall contributions to stiffness should be further explored. Further data on out-of-plane wall testing and performance to failure under wave loading are needed to validate nonlinear FE models when predicting structural collapses. In addition, other FE models or combined discrete elements method (DEM) formulation can be used to simulate elastic truss and beam elements

CRediT authorship contribution statement

Mohammad S. Alam: Formal analysis, Software, Investigation, Data curation, Writing – original draft, Visualization. Andre R. Barbosa: Conceptualization, Methodology, Validation, Funding acquisition, Writing – original draft, Writing – review & editing, Project administration. Ignace Mugabo: Visualization, Investigation. Daniel T. Cox: Conceptualization, Writing – review & editing, Project administration, Funding acquisition. Hyoungsu Park: Supervision, Writing – review & editing. Dayeon Lee: Formal analysis, Software, Visualization. Sungwon Shin: Supervision, Writing – review & editing.

Declaration of Competing Interest

The authors declare that they have no known competing financial interests or personal relationships that could have appeared to influence the work reported in this paper.

Data availability

Data is available on DesignSafe-CI. Hydrodynamic test data is publicly available in Cox et al. [20] at DesignSafe-CI.https://doi.org/10.17603/ds2-8evm-1y60 v1 and structural testing and system identification data is available in Barbosa et al. [9] at DesignSafe-CI.https://doi.org/10.17603/ds2-v287-t615v1.

Acknowledgements

The material presented in this study is based on financial support by the National Science Foundation (NSF) under awards 1519679 and 1661315. Any opinions, findings, conclusions, or recommendations expressed in this study are those of the authors and do not necessarily reflect the views of NSF. The authors gratefully acknowledge Sean Duncan, Pedro Lomonaco, and Tim Maddux who helped with the experimental setup for out-of-water dynamic structural characterization tests and in-water hydrodynamic tests at the wave basin of NSF-NHERI facility at Oregon State University.

References

- [1] Adhikari P, Abdelhafez MA, Dong Y, Guo Y, Mahmoud HN, Ellingwood BR. Achieving Residential Coastal Communities Resilient to tropical Cyclones and Climate Change. Frontiers in Built Environment 2021;6:576403.
- [2] Alam MS, Barbosa AR, Scott MH, Cox DT, van de Lindt JW. Development of Physics-Based Tsunami Fragility Functions Considering Structural Member Failures. J Struct Eng 2018;144(3):04017221.
- [3] Alam MS, Winter AO, Galant G, Shekhar K, Barbosa AR, Motley MR, et al. Tsunami-Like Wave-Induced Lateral and Uplift Pressures and forces on an Elevated Coastal Structure. J Waterw Port Coast Ocean Eng 2020;146(4):04020008.
- [4] Aloisio A, Pasca DP, Santis YD, Hillberger T, Giordano PF, Rosso MM, et al. Vibration issues in timber structures: A state-of-the-art review. Journal of Building Engineering 2023;76(2023):107098. https://doi.org/10.1016/j. iobs.2023.107098
- [5] ARTEMIS Modal (2017). Available online at: http://www.svibs.com/products/ ARTEMIS Modal.aspx (accessed April 15, 2020).
- [6] Asgarieh E, Moaveni B, Barbosa AR, Chatzi E. Nonlinear model calibration of a shear wall building using time and frequency data features. Mech Syst Sig Process 2017;85:236–51.
- [7] Astroza R, Ebrahimian H, Li Y, Conte JP. Bayesian Nonlinear Structural FE Model and Seismic Input Identification for Damage Assessment of Civil Structures. Mech Syst Sig Process 2017;93:661–87.
- [8] Atc. Recommended Modeling Parameters and Acceptance Criteria for Nonlinear Analysis in Support of Seismic Evaluation, Retrofit, And Design (NIST GCR 17–917-45). National Institute of Standards and Technology 2017. https://doi.org/ 10.6028/NIST.GCR.17-917-45.
- [9] Barbosa, A. Cox, D. Alam, M. Mugabo, I. Park, H. Duncan, S. Lomonaco, P. (2021a). Static and Dynamic Structural Characterization Tests of Wave Basin Hydrodynamic Experiments of Scaled Wood Frame Shear-Wall Residential Buildings", In Progressive Damage and Failure of Wood-Frame Coastal Residential Structures Due to Hurricane Surge and Wave Forces. DesignSafe-CI. https://doi.org/10.17603/ ds2-v287-t615.
- [10] Barbosa AR, Rodrigues LG, Sinha A, Higgins C, Zimmerman RB, Breneman S, et al. Shake-Table Experimental Testing and Performance of Topped and Untopped Cross-Laminated Timber Diaphragms. J Struct Eng 2021;147(4):04021011.
- [12] Blake ES, Kimberlain TB, Berg RJ, Cangia Losi JP, Beven II JL. Tropical Cyclone Report Hurricane Sandy 2013;AL182012:22–9. https://doi.org/10.1017/ CB09781107415324.004.
- [13] Brincker, R., Andersen, P. (2006). Understanding stochastic subspace identification. In Proceedings of the 24th International Modal Analysis Conference, 461–466. St. Louis. MO.
- [14] Brincker R, Zhang L, Andersen P. Modal Identification of Output-Only Systems Using Frequency Domain Decomposition. Smart Mater Struct 2001;10:441–5. https://doi.org/10.1088/0964-1726/10/3/303.
- [15] Cch. City and County of Honolulu Building Code. Department of Planning and Permitting of Honolulu Hawai'i; 2000.
- [16] Chock G, Carden L, Robertson I, Olsen M, Yu G. Tohoku Tsunami-Induced Building Failure Analysis with Implications for US Tsunami and Seismic Design Codes. Earthq Spectra 2013;29(s1):S99–126.
- [17] Chopra AM. Dynamics of structures: Theory and Applications to Earthquake Engineering, Prentice Hall; 2001. ISBN-10: 2001 0130869732.
- [18] Como A, Mahmoud H. Numerical Evaluation of Tsunami Debris Impact Loading on Wooden Structural Walls. Eng Struct 2013;56:1249–61.
- [19] Cortes, M., P. Arora, L. Ceferino, H. Ibrahim, D. Istrati, D. Reed, D. Roueche, A. Safiey, T. Tomiczek, I. Zisis, M. Alam, T. Kijewski-Correa, D. Prevatt, and I. Robertson (2022). "StEER: Hurricane Ian Preliminary Virtual Reconnaissance Report (PVRR)." Designsafe-Cl. https://doi.org/10.17603/ds2-kc9k-s242.
- [20] Cox, D. Barbosa, A. Alam, M. Park, H. Duncan, S. Lomonaco, P. (2021). Hydrodynamic Tests on Physical Models of Scaled Wood Frame Shear-Wall Residential Buildings. In Progressive Damage and Failure of Wood-Frame Coastal Residential Structures Due to Hurricane Surge and Wave Forces. DesignSafe-CI. https://doi.org/10.17603/ds2-8evm-1y60.
- [21] Cox D, Arikawa T, Barbosa A, Guannel G, Inazu D, Kennedy A, et al. Hurricanes Irma and Maria post-event survey in US Virgin Islands. Coast Eng J 2019;61(2): 121–34. https://doi.org/10.1080/21664250.2018.1558920.
- [22] Dean PK, Shenton HW. Experimental Investigation of the Effect of Vertical Load on the Capacity of Wood Shear Walls. J Struct Eng 2005;131(7):1104–13. https://doi. org/10.1061/(ASCE)0733-9445(2005)131:7(1104).
- [23] Duncan S, Cox D, Barbosa AR, Lomónaco P, Park H, Alam MS, et al. Physical Modeling of Progressive Damage and Failure of Wood-Frame Coastal Residential Structures Due to Surge and Wave Forces. Coast Eng 2021;169:103959.
- [24] Fema p-55.. Coastal Construction Manual-Volume-I. FEMA; 2011.
- [25] Folz B, Filiatrault A. Cyclic Analysis of Wood Shear Walls. J Struct Eng 2001;127 (4):433–41. https://doi.org/10.1061/(ASCE)0733-9445(2001)127:4(433).

- [26] Folz B, Filiatrault A. Seismic Analysis of Wood Frame Structures. I: Model Formulation. J Struct Eng 2004;130(9):1353–60. https://doi.org/10.1061/(ASCE) 0733-9445(2004)130-9(1353)
- [27] Folz, B., Filiatrault, A. (2004b). Seismic Analysis of Wood Frame Structures. II: Model Implementation and Verification. Journal of Structural Engineering, 130(9), 1361–1370. https://doi.org/10.1061/(ASCE)0733-9445(2004)130:9(1361).
- [28] Fritz HM, Blount CD, Thwin S, Thu MK, Chan N. Cyclone Nargis Storm Surge in Myanmar. Nat Geosci 2009;2(7):448–9. https://doi.org/10.1038/ngeo558.
- [29] Gres, S., Andersen, P., Hoen, C., Damkilde, L. (2019). Orthogonal Projection-Based Harmonic Signal Removal for Operational Modal Analysis. In Structural Health Monitoring, Photogrammetry and DIC, Volume 6. Conference Proceedings of the Society for Experimental Mechanics Series, Eds. C. Niezrecki and J. Baqersad (Cham: Springer).
- [30] Hatzikyriakou A, Lin N. Assessing the Vulnerability of Structures and Residential Communities to Storm Surge: An Analysis of Flood Impact During Hurricane Sandy, Frontiers in Built Environment 2018;4:4.
- [31] Hatzikyriakou A, Lin N, Gong J, Xian S, Hu X, Kennedy A. Component-Based Vulnerability Analysis for Residential Structures Subjected to Storm Surge Impact from Hurricane Sandy. nat Hazard Rev 2016;17(1):05015005. https://doi.org/ 10.1061/(ASCE)NH.1527-6996.0000205.
- [32] Higuera P, Losada LJ, Lara JL. Three-dimensional Numerical Wave Generation with Moving Boundaries. Coast Eng 2015;101:35–47.
- [33] IRC. International Residential Code for One and Two-Family Dwellings. Washington DC, USA: International Code Council (ICC); 2018.
- [34] JCSS (2006). Joint Committee on Structural Safety Probabilistic Model Code. URL: https://www.jcss-lc.org/jcss-probabilistic-model-code/ [accessed Dec. 26, 2021].
- [35] Kennedy A, Rogers S, Sallenger A, Gravois U, Zachry B, Dosa M, et al. Building Destruction from Waves and Surge on the Bolivar Peninsula during Hurricane Ike. J Waterw Port Coast Ocean Eng 2011;137(3):132–41. https://doi.org/10.1061/ (ASCE)WW.1943-5460.0000061.
- [36] Lee D, Park H, Ha T, Shin S, Cox DT. Numerical modeling of hydrodynamics on an elevated residential structure from varied wave and surge conditions using OpenFOAM. Coast Eng 2022;178:104204. https://doi.org/10.1016/j. coastaleng.2022.104204. ISSN 0378-3839.
- [38] Linton D, Gupta R, Cox D, van de Lindt J. Load Distribution in Light-Frame Wood Buildings under Experimentally Simulated Tsunami Loads. J Perform Constr Facil 2015;29(1):04014030. https://doi.org/10.1061/(ASCE)CF.1943-5509.0000487.
- [39] Linton D, Gupta R, Cox D, van de Lindt J, Oshnack ME, Clauson M. Evaluation of Tsunami Loads on Wood-Frame Walls at Full-scale. J Struct Eng 2013;139(8): 1318–25. https://doi.org/10.1061/(ASCE)ST.1943-541X.0000644.
- [40] Magalhães, F., Brincker, R., Cunha, Á., Caetano, E., Brincker, R. (2007). Damping Estimation Using Free Decays and Ambient Vibration Tests. In Proceedings of the 2nd International Operational Modal Analysis Conference, 513–521, Copenhagen, Denmark.
- [41] Magalhães F, Cunha Á, Caetano E, Brincker R. Damping Estimation Using Free Decays and Ambient Vibration Tests. Mech Syst Sig Process 2010;24(5):1274–90.
- [42] Matlab, Version R2020a, Natick, Massachusetts: The MathWorks Inc.: 2020.
- 43] McKenna F, Scott MH, Fenves GL. Nonlinear Finite-Element Analysis Software

 Architecture Using Object Composition J Comput Civ Fng 2010;24(1):95–107
- Architecture Using Object Composition. J Comput Civ Eng 2010;24(1):95–107.
 [44] Mendelsohn R, Emanuel K, Chonabayashi S, Bakkensen L. The Impact of Climate Change on Global Tropical Cyclone Damage. Nat Clim Chang 2012;2(3):205–9. https://doi.org/10.1038/nclimate1357.
- [45] Moaveni B, Barbosa AR, Conte JP, Hemez FM. Uncertainty Analysis of System Identification Results Obtained for A Seven-Story Building Slice Tested on the UCSD-NEES Shake Table. Struct Control Health Monit 2014;21(4):466–83.
- [46] Mori N, Shimura T, Yasuda T, Mase H. Multi-Model Climate Projections of Ocean Surface Variables Under Different Climate Scenarios—Future Change of Waves, Sea Level and Wind. Ocean Eng 2013;71:122–9. https://doi.org/10.1016/j. oceaneng.2013.02.016.
- [47] Moris JP, Kennedy AB, Westerink JJ. Tsunami Wave Run-Up Load Reduction Inside a Building Array. Coast Eng 2021;103910.
- [48] Mugabo I, Barbosa AR, Riggio M. Dynamic Characterization and Vibration Analysis of a Four-Story Mass Timber Building. Frontiers in Built Environment 2019;5. https://doi.org/10.3389/fbuil.2019.00086.
- [49] Mugabo I, Barbosa AR, Sinha A, Higgins C, Riggio M, Pei S, et al. System Identification of UCSD-NHERI Shake-Table Test of Two-Story Structure with Cross-Laminated Timber Rocking Walls. J Struct Eng 2021;147(4):04021018.
- [50] Nanto DK, Cooper WH, Donnelly JM. Japan's 2011 Earthquake and Tsunami: Economic Effects and Implications for the United States. Washington, DC: Congressional Research Service for Congress; 2011.
- [51] National Instruments (2013). SignalExpress: Getting Started with SignalExpress. Austin, TX. Available online at: http://www.ni.com/pdf/manuals/373873h.pdf, accessed: 12/26/2021.
- [52] NOAA and NHC (2018). Costliest US Tropical Cyclones Tables Updated. NOAA Technical Memorandum NWS NHC-63. Available online at: https://www.nhc. noaa.gov/news/UpdatedCostliest.pdf, accessed: 12/26/2021.

- [53] Park H, Do T, Tomiczek T, Cox DT, van de Lindt JW. Numerical Modeling of Non-Breaking, Impulsive Breaking, And Broken Wave Interaction with Elevated Coastal Structures: Laboratory Validation and Inter-Model Comparisons. Ocean Eng 2018; 158-78-98
- [54] Pei S, van de Lindt JW. User's manual for SAPWood for Windows, Version 1.0. SAPWood program user's manual. Colorado: Colorado State University; 2007.
- [55] Pei S, van de Lindt JW, Barbosa AR, Berman JW, McDonnell E, Daniel Dolan J, et al. Experimental Seismic Response of a Resilient 2-Story Mass-Timber Building with Post-Tensioned Rocking Walls. J Struct Eng 2019;145(11):04019120.
- [56] Pei S, van de Lindt JW, Wehbe N, Liu H. Experimental Study of Collapse Limits for Wood Frame Shear Walls. J Struct Eng 2013;139(9):1489–97.
- [57] Reis C, Clain S, Figueiredo J, Barbosa AR, Baptista MA, Lopes M. Experimentally Validated Numerical Models to Assess Tsunami Hydrodynamic Force on an Elevated Structure. Eng Struct 2021;249:113280.
- [58] Robertson IN, Riggs HR, Yim SC, Young YL. Lessons from Hurricane Katrina Storm Surge on Bridges and Buildings. J Waterw Port Coast Ocean Eng 2007;133(6): 463–83. https://doi.org/10.1061/(ASCE)0733-950X(2007)133:6(463).
- [59] Rodrigues LG, Branco JM, Neves LA, Barbosa AR. Seismic Assessment of a Heavy-Timber Frame Structure with Ring-Doweled Moment-Resisting Connections. Bull Earthq Eng 2018;16(3):1341–71.
- [60] Rosowsky DV, Bulleit WM. Load Duration Effects in Wood Members and Connections: Order Statistics and Critical Loads. Struct Saf 2002;24(2–4):347–62.
- [61] Saatcioglu, M., Ghobarah, A., & Nistor, I. (2006). Performance of Structures Affected by the 2004 Sumatra Tsunami in Thailand and Indonesia. In T. Murty, U. Aswathanarayana, & N. Nirupama (Eds.), The Indian Ocean Tsunami (pp. 297–321). Taylor & Francis. https://doi.org/10.1201/9780203964439.pt4.
- [62] Shekhar K, Winter AO, Alam MS, Arduino P, Miller GR, Motley MR, et al. Conceptual Evaluation of Tsunami Debris Field Damming and Impact Forces. J Waterw Port Coast Ocean Eng 2020;146(6):04020039.
- [63] Sogut E, Velioglu Sogut D, Farhadzadeh A. Overland Wave Propagation and Load Distribution among Arrays of Elevated Beachfront Structures. J Waterw Port Coast Ocean Eng 2020;146(4):04020016.
- [64] Tomiczek T, Kennedy A, Rogers S. Collapse Limit State Fragilities of Wood-Framed Residences from Storm Surge and Waves During Hurricane Ike. Journal of Waterway, Port, Coastal, Ocean Eng 2014;140(1):43–55. https://doi.org/10.1061/ (ASCE)WW.1943-5460.0000212.
- [65] Tomiczek T, Kennedy A, Zhang Y, Owensby M, Hope ME, Lin N, et al. Hurricane Damage Classification Methodology and Fragility Functions Derived from Hurricane Sandy's Effects in Coastal New Jersey. J Waterw Port Coast Ocean Eng 2017;143(5):04017027.
- [66] Tomiczek T, Wyman A, Park H, Cox DT. Modified Goda Equations to Predict Pressure Distribution and Horizontal Forces for Design of Elevated Coastal Structures. J Waterw Port Coast Ocean Eng 2019;145(6):04019023.
- [67] van de Lindt JW, Furley J, Amini MO, Pei S, Tamagnone G, Barbosa AR, et al. Experimental Seismic Behavior of a Two-Story CLT Platform Building. Eng Struct 2019;183:408–22.
- [68] van de Lindt JW, Gupta R, Garcia RA, Wilson J. Tsunami Bore Forces on a Compliant Residential Building Model. Eng Struct 2009;31(11):2534–9. https://doi.org/10.1016/j.engstruct.2009.05.017.
- [69] van de Lindt JW, Pei S, Liu H, Filiatrault A. Three-Dimensional Seismic Response of a Full-Scale Light-Frame Wood Building: Numerical Study. J Struct Eng 2010;136 (1):56–65. https://doi.org/10.1061/(ASCE)ST.1943-541X.0000086.
- [70] Wilson JS, Gupta R, van de Lindt JW, Clauson M, Garcia R. Behavior of a One-Sixth Scale Wood-Framed Residential Structure under Wave Loading. J Perform Constr Facil 2009;23(5):336–45. https://doi.org/10.1061/(ASCE)CF.1943-5509.000039.
- [71] Winter AO, Alam MS, Shekhar K, Motley MR, Eberhard MO, Barbosa AR, et al. Tsunami-like wave forces on an elevated coastal structure: Effects of flow shielding and channeling. J Waterw Port Coast Ocean Eng 2020;146(4):04020021.
- [72] Handbook W. Wood as an Engineering Material. Madison, WI: Forest Products Laboratory; United States Department of Agriculture Forest Service; 2010.
- [73] Xian S, Lin N, Hatzikyriakou A. Storm Surge Damage to Residential Areas: A Quantitative Analysis for Hurricane Sandy in Comparison with FEMA Flood Map. Nat Hazards 2015;79(3):1867–88. https://doi.org/10.1007/s11069-015-1937-x.
- [74] Yeh SC, Rogers SM, Tung CC, Kasal B. Behavior of Breakaway Walls Under Wave Action. J Struct Eng 1999;125(10):1162–9.
- [75] Yu, C., Cox, D., Barbosa, A.R., Che, E., Duncan, S., Tomiczek, T. (2019). Progressive Damage Assessment of On-Slab and Elevated Structures from Storm Surge and Waves Using LiDAR in a Laboratory Wave Basin. Undergraduate Research Experience (REU) Report. NHERI 2019: DesignSafe-CI. https://doi.org/ 1T0.17603/ds2-0rky-9w25.
- [76] Filiatrault A, Fischer D, Folz B, Uang CM. Seismic testing of two-story woodframe house: Influence of wall finish materials. J Struct Eng 2002;128(10):1337–45.
- [77] Reis C, Barbosa AR, Figueiredo J, Clain S, Lopes M, Baptista MA. Smoothed particle hydrodynamics modeling of elevated structures impacted by tsunami-like waves. Eng Struct 2022;270:114851. https://doi.org/10.1016/j.engstruct.2022.114851. ISSN 0141-0296.